This is the Accepted manuscript.
Seunghye Lee,, Qui X. Lieu, Thuc P. Vo, Joowon Kang, Jaehong Lee, Topology optimization using super-resolution image reconstruction methods, Advances in Engineering Software, Volume 177, 2023, 103413, ISSN 0965-9978, https://doi.org/10.1016/j.advengsoft.2023.103413.

Topology optimization using super-resolution image reconstruction methods

Seunghye Lee[a,1], Qui X. Lieu[b,c,2], Thuc P. Vo[d,3], Joowon Kang[e,4], Jaehong Lee[a,*]

[a] *Deep Learning Architecture Research Center, Department of Architectural Engineering, Sejong University 209, Neungdong-ro, Gwangjin-gu, Seoul 05006, Republic of Korea*
[b] *Faculty of Civil Engineering, Ho Chi Minh City University of Technology (HCMUT) 268 Ly Thuong Kiet Street, District 10, Ho Chi Minh City, Vietnam*
[c] *Vietnam National University Ho Chi Minh City (VNU-HCM) Linh Trung Ward, Thu Duc City, Ho Chi Minh City, Vietnam*
[d] *School of Computing, Engineering and Mathematical Sciences, La Trobe University Bundoora, VIC 3086, Australia*
[e] *School of Architecture, Yeungnam University 280 Daehak-Ro, Gyeongsan, Gyeongbuk 38541, Republic of Korea*

Abstract

This paper proposes a new topology optimization method to obtain super-resolution images without increasing mesh refinement by using various methods. For traditional process, low-resolution (LR) images are fed into the Solid Isotropic Material with Penalization (SIMP) and Optimality Criteria (OC) methods. Here, the trained super-resolution images are added to the inner loops to reconstruct the topology and used to obtain high-resolution (HR) images from the LR images at the end of each iteration. After finishing the reconstruction process, the main topology optimization method recovers the original size images from the HR images for the next iteration. Several examples are presented to demonstrate the effectiveness of the proposed method. The final topologies provide noticeably improvement over those of typical SIMP method and create a much sharper and higher contrast images. Moreover, the proposed strategy using the super-resolution image reconstruction methods can give valuable innovation for conventional topology optimization process.

Keywords: Super-resolution, Topology optimization, Single-material, Multi-material, SIMP

[*] Professor, Ph.D, corresponding author. Tel.:+82-2-3408-3287; fax:+82-2-3408-4331
Email address: `jhlee@sejoing.ac.kr` (Jaehong Lee)
[1] Assistant professor, Ph.D
[2] Lecturer, Ph.D
[3] Associate professor, Ph.D
[4] Professor, Ph.D

1. Introduction

Optimization problems of structures are roughly classified into three categories: sizing, shaping, and topology optimization (TO) [1]. Among them, TO needs non-linear mathematical programming methods to obtain the optimal shape [2] and the first paper related to this was published over a century ago [3]. The main purpose is to find the optimal layout of the structure by considering the best structural performance [4]. The first general theory of TO, which is optimal layout theory, was formulated by Rozvany and Prager [5]. Bendsøe and Kikuchi [6] published a landmark paper, which was based on the optimal material distribution in a predefined design domain by the homogenization method. The TO topics have been developed and innovated by many researchers all over the world [7].

The density-based approach by Bendsøe [8] is prone to problems with checkerboards and mesh dependency if there are not any regularization schemes [9]. The solutions using that approach can roughly be divided into three categories, namely, filtering methods [10–14], constraint methods [12, 15–22], and other alternative methods [23–29]. The checkerboards can be removed through smoothing or inhibited methods by using higher-order finite elements [30]. Results of the density filtering methods have grey transition regions between solid (black) and void (white) areas as shown in Figure 1. The grey transition regions depend on the filter size and discretization of the problems. In the ‘filtered, penalized artificial material method’ [15], a density of material varies continuously between 1 and 0. The regions contain intermediate volume fractions along the boundary. In order to ensure existence of solutions in the numerical methods, multiple phase projection method [31] can be used as filter technique.

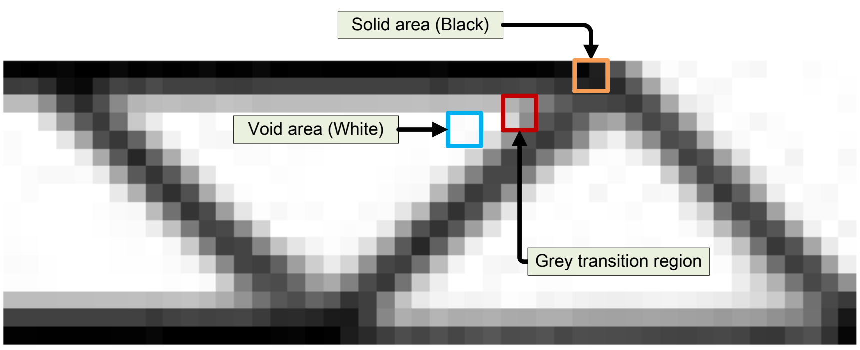

Figure 1: The results of the density filtering method with grey transition regions between solid (black) and void (white) areas.

There have been attempts to apply deep learning methods to the TO problems. Li et al. [32] used Convolutional Neural Networks (CNNs) and Generative Adversarial Networks (GANs) [33] to construct mapping images and generate more images. Yu et al. [34] also introduced both CNNs and GANs into a near-optimal topological design to reduce computational cost dramatically. Sasaki and Igarashi [35] reduced the computing costs by using CNNs in the learning phase prior to the optimization step. Rawat and Shen [36] introduced another GAN method, namely, Conditional Wasserstein Generative Adversarial Networks (CWGANs) to replicate the conventional TO algorithms in an extremely computationally inexpensive way. Sosnovik and Oseledets [37] proposed a new TO method by using the CNNs and an encoder-decoder algorithm to enhance the image resolution. However, only few studies have applied super-resolution (SR) techniques as the filter of TO problems. Li et al. [38] proposed a Super-Resolution Generative Adversarial Network (SRGAN) for predicting the refined structure in High-Resolution (HR). They only used SRGAN as the last step for refining HR after typical GANs produced a Low-Resolution (LR) image. Xue et al. [39] used the super-resolution convolutional neural network (SRCNN) technique in the framework of SIMP. The pooling strategy in the CNN process is used for the image reconstruction. Wang et al. [40] used CNN method to obtain an accurate high-resolution structure images. A TO via neural reparameterization framework (TONR) was proposed to solve various problems using a inverting representation of image and physics-informed neural network methods [41]. However, there are few studies that apply the state-of-the-art SR method.

The super-resolution (SR) image is an important class of image processing techniques in computer vision. The SR image reconstruction method aims to convert a given low-resolution (LR) image to a corresponding high-resolution (HR) one with refined details. Its concept is suitable for the TO methods, which deal with images of structural shapes. It can be broadly divided into two main categories: traditional and deep learning methods [42]. In recent years, with the rapid development of deep learning techniques, SR models have been actively explored and often achieve the state-of-the-art performance on various benchmarks [43]. Various deep learning based SR methods are used to enhance LR images of optimization processes, namely, an Enhanced Deep Super-Resolution network (EDSR) [44], Wide-Activation Deep Super-Resolution (WDSR) [45], and Super-Resolution Generative Adversarial Network (SRGAN) [46], Fast Super-Resolution Convolutional Neural Network (FSRCNN) [47], Efficient Sub-Pixel Convolutional Neural Network

(ESPCN) [48], and Laplacian Pyramid Super-Resolution Network (LapSRN) [49]. New HR topology images can be then reconstructed from the LR images with a $4\times$ upscaling factor.

This paper proposes a new topology optimization approach, in which (SR) image reconstruction is embedded within a conventional TO process and the generated SR procedures are used as a filter technique. The main purpose is to reduce the compliance values in the whole processes and to obtain optimized designs of structures. The SR image reconstruction step is added to the TO process, the HR ones are then reflected back into the main process. Several methods such as EDSR, WDSR, SRGAN, FSRCNN, ESPCN, and LapSRN are used. In the proposed method, the trained SR methods are added to the inner loops of the two types of processes, namely, a single-material and a multi-material topology optimization methods, to upscale LR images. Several examples are presented to demonstrate the effectiveness of the proposed method. The proposed topology optimization algorithm achieves better results compared with the traditional method, Solid Isotropic Material with Penalization (SIMP).

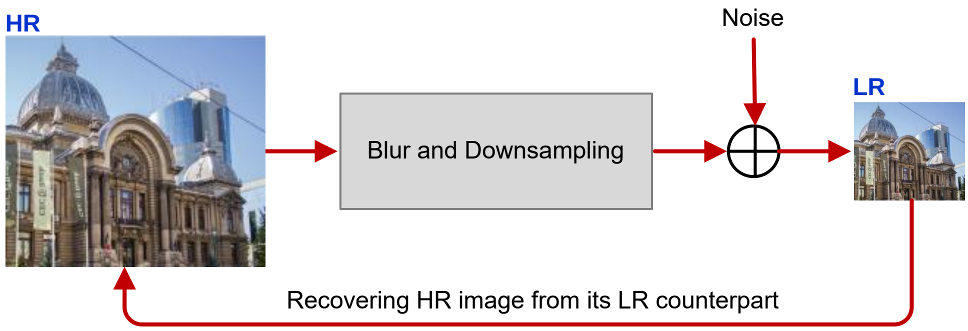

Figure 2: Overview of the overall framework of SISR.

2. Super-resolution image reconstruction methods

2.1. Related work

The Single Image Super-Resolution (SISR) aims to reconstruct a HR image from a LR one [50]. It can be categorized into nine groups ([42]), which are linear, residual and recursive networks, multi-branch and progressive reconstruction designs, densely connected, attention-based and multiple degradation handling networks as well as GAN. If LR image and the corresponding HR one are denoted by $\mathbf{y}$ and $\mathbf{x}$, their relationship is given as [50]:

, Thuc P. Vo, Joowon Kang, Jaehong Lee, Topology optimization using super-resolution image reconstruction methods, Advances in Engineering Software, Volume 177, 2023, 103413, ISSN 09

$$\mathbf{y} = (\mathbf{x} \otimes \mathbf{k}) \downarrow_s + \mathbf{n} \tag{1}$$

where $(\mathbf{x} \otimes \mathbf{k})$ is the convolution operation between the blurring kernel $\mathbf{k}$ and the unknown HR image. The notation $\downarrow_s$ indicates a downsampling operation with a scaling factor s. The variable $\mathbf{n}$ denotes the independent noise term. Figure 2 shows the overview of the overall framework of the SISR.

SISR using a variety of deep learning techniques have been actively explored [51]. SRCNN approximates the complex mapping between the LR and HR images in an end-to-end manner [52]. It minimizes the difference between the output reconstructed HR images and ground truth ones. However, deep layer structures in SRCNN make it difficult to learn the network parameters effectively due to vanishing gradient. In order to increase depth and width of the architectures, Very Deep Super-Resolution (VDSR) is the first one used in SISR [53]. To train VDSR, a relatively high initial learning rate and gradient clipping were used to speed up convergence and prevent the gradient explosion problem. However, a degradation problem has been exposed when deeper networks can start to converge [54]. To overcome this problem, ResNet [55] incorporates skip-connections between layers to avoid gradients vanishing. ResNet uses residual networks to ease the training networks that are substantially deeper than previous SR method. It adopts Batch Normalization (BN) between the convolution layer and activation functions [56]; the BN layer normalizes the input of activation functions. The residual networks require a residual mapping to restore the missing high-frequency details and make it feasible to design very deep networks [57]. SRGAN uses the original GAN models for image SR. With two components including a generator and discriminator, it provides a powerful framework for generating fake images with perceptual quality [46].

2.2. Enhanced Deep Super-Resolution network (EDSR)

EDSR consists of multiple residual blocks and removes the parts in the residual structure for flexibility while ResNet adopts the batch normalization between the convolution layer and activation functions to normalize the features [44]. The residual blocks have two convolutional layers connected with a Rectified Linear Unit activation function (ReLU) [58]. Since the inner representation is highly abstract and can be insensitive to the shift introduced by the batch normalization layers, it is better to remove from the whole architectures. Moreover, EDSR increases the number of output features of each layer and uses pre-training strategy to improve the final performances [50]. 16 residual blocks for 4× upscaling are used in this study.

2.3. Wide-activation Deep Super-Resolution (WDSR)

WDSR can improve EDSR with three aspects, namely, wide activation, weight normalization in training, and simplified global residual pathway [45]. In the SR residual network of WDSR architecture, it has a slim identify mapping pathway with wider channels, 2× to 4×, for WDSR-A models or 6× to 9× channels for WDSR-B models before activations in each residual block. In this study, a WDSR-B model with a 6× expansion factor and 32 residual blocks are used to train the architecture for 4× upscaling.

2.4. Super-Resolution on Generative Adversarial Network (SRGAN)

GANs, which are very effective methods for SR reconstruction, consist of a generator network, which attempts to generate images from smaller size images, and discriminator network, which determines whether the generated images are real or fake [59]. SRGAN uses an adversarial objective function, which promotes super-resolved output [46] and takes the architecture of GANs; the generator network has residual blocks, similarly to EDSR and VDSR. However, the residual blocks consist of two convolutional layers, two batch normalization layers, and Parametric Rectified Linear Unit (PReLU) activation function [60]. In this study, 16 residual blocks, each of which consists of convolutional layer, are used and follow the architectural guidelines of the discriminator network summarized by Ledig et al. [46]. The discriminator network contains eight convolutional layers. The final sigmoid activation function is used to obtain a probability for sample classification.

2.5. Fast Super-Resolution Convolutional Neural Networks (FSRCNN)

In spite of its superior performance, the original SRCNN method demands the high computational cost. In FSRCNN method, SRCNN [61] is modified to accelerate the current method. A deconvolution layer is introduced at the end of the network of FSRCNN and thereby the mapping is learned directly from the LR image without interpolation processes. The mapping layer is reformulated by shrinking the input feature dimension, and smaller filter sizes but more mapping layers are applied thereafter. These strategies can accelerate the original SRCNN method while still keeping its exceptional performance.

2.6. Efficient Sub-Pixel Convolutional Neural Network (ESPCN)

In ESPCN method, an efficient sub-pixel convolution layer is added to learn the upscaling operation for images. The upscaling layer is only located at the last of the network. It indicates that each LR image is directly fed into the network and feature extraction is then occurred in LR spaces. In other words, the process of the ESPCN ensures that the previous convolution operations are performed on LR images, which improves image reconstruction efficiency. By doing so, a smaller size filter can be used to integrate the same information while maintaining a given contextual area. Finally, the computational complexity of the overall SR operation can be reduced.

2.7. Laplacian Pyramid Super-Resolution Network (LapSRN)

LapSRN consists of a feature extraction branch which uses convolutional layers to extract non-linear feature maps from LR input images, and an image reconstruction branch which takes the sub-band residuals from the feature extraction branch. In the feature extraction process, two convolutional layers are used to upsample the feature maps and to predict the sub-band residuals, respectively. Then the image reconstruction process takes the sub-band residuals to reconstruct HR images through element-wise addition. Because the LapSRN directly extracts features from the LR input images, the computational complexity can be reduced.

3. Performance evaluation of super-resolution reconstruction methods

The average pixels from variety of datasets available, which are sets of animal, building, food, landscape, people, plant, etc., have wide ranges from $58,853$ of T91 dataset [62] to $11,577,492$ of L20 dataset [63]. Because the pixel size of LR topology image dealt with in this paper is quite small compared to those image dataset mentioned above, various SR reconstruction methods should be tried to find the most efficient one for this proposed approach. Prior to applying the pre-trained six SR reconstruction methods, one of the public image datasets and two samples of the topology examples were evaluated using Image Quaility Assessment (IQA) methods.

3.1. Image Quality Assessment (IQA)

The SR techniques need IQA methods to assign perceptual quality scores to the tested images. In general, they can be divided into two parts, namely, subjective and objective methods [64]. The subjective methods are based on human perception and operate without reference to explicit criteria. On the other hand, the objective methods are based on comparisons using explicit numerical criteria [65]. The subjective methods are usually time-consuming and expensive, while the objective ones are often unable to capture the human visual perception.

The objective IQA can be divided into three types: full-reference, reduced-reference, and no-reference [64]. In the full-reference type, a complete reference image is assumed to be known, while the no-reference methods do not use any reference images. The reduced-reference type requires a limited number features extracted from the reference for the IQA task. In this paper, two well-known full-reference quality metrics are used, namely, Peak Signal-to-Noise Ratio (PSNR) and Structure Similarity Index Method (SSIM).

3.1.1. Peak Signal-to-Noise Ratio (PSNR)

PSNR is one of the most popular reconstruction quality measurement. It is defined via the maximum pixel value, L, and the Mean-Squared Error (MSE) between two images. Given a reference image I with N pixels and a reconstruction image $\hat{I}$, the PSNR between two images are defined as follows:

$$\mathrm{PSNR}(I,\hat{I}) = 10\log_{10}\left(\frac{L^2}{\mathrm{MSE}(I,\hat{I})}\right) \tag{2}$$

$$\mathrm{MSE}(I,\hat{I}) = \frac{1}{N}\sum_{i=1}^{N}\left(I(i)-\hat{I}(i)\right)^2 \tag{3}$$

where L equals to 255 in general cases using 8-bit representations. The notation $I(i)$ represents the intensity of the i-th pixel of image I.

The PSNR value approaches infinity as the MSE approaches zero, which implies that a higher PSNR value indicates a higher image quality [65]. In image compression quality degradation, the PSNR value varies from 30 to 50 dB for 8-bit data representation.

3.1.2. Structure Similarity Index Method (SSIM)

SSIM proposed by Wang et al. [64] measures the structural similarity between images, based on independent comparisons in terms of luminance masking, contrast masking, and structures. The luminance masking and contrast masking are terms where the distortion is less visible in the edges and texture of images, respectively. The structure comparison function measures the correlation coefficient between two images. Given a reference image I with N pixels, the mean luminance (μ_I) and the standard deviation of the image intensity (σ_I) are defined as follows [28]:

$$\mu_I = \frac{1}{N}\sum_{i=1}^{N} I(i) \tag{4}$$

$$\sigma_I = \sqrt{\frac{1}{N-1}\sum_{i=1}^{N}\left(I(i)-\mu_I\right)^2} \tag{5}$$

By using the two equations, the SSIM is defined as:

$$\mathrm{SSIM}(I,\hat{I}) = l(I,\hat{I})c(I,\hat{I})s(I,\hat{I}) \tag{6}$$

where

$$l(I,\hat{I}) = \frac{2\mu_I\mu_{\hat{I}} + C_1}{\mu_I^2 + \mu_{\hat{I}}^2 + C_1} \tag{7}$$

$$c(I,\hat{I}) = \frac{2\sigma_I\sigma_{\hat{I}} + C_2}{\sigma_I^2 + \sigma_{\hat{I}}^2 + C_2} \tag{8}$$

$$s(I,\hat{I}) = \frac{\sigma_{I\hat{I}} + C_3}{\sigma_I\sigma_{\hat{I}} + C_3} \tag{9}$$

The term $l(I,\hat{I})$, $c(I,\hat{I})$, and $s(I,\hat{I})$ represent the luminance, contrast, and structure comparison functions, respectively. Note that $\sigma_{I\hat{I}}$ is the covariance between I and $\hat{I}$. The positive constants C_1, C_2, and C_3 are used to avoid a null denominator. The SSIM index varies from 0 to 1. A value of 0 and 1 indicate no correlation between two images and $I = \hat{I}$, respectively.

3.2. ×4 Super-resolution results with six algorithms

Figure 3 shows the ×4 SR results of the "Zebra" example from **Set14** dataset [66]. Most SR methods evaluate their models on the standard benchmark datasets. For comparing the PSNR and SSIM values, the original image is 48×16 pixels in size which is resized to 192×64 pixels by using bi-cubic interpolation. The result of FSRCNN shows the highest PSNR value and ESPCN and LapSRN give the best SSIM value. However, because structural images are used in this paper to enhance the TO work, two images of single- and multi-material topologies are compared Figures 4 and 5. For single-material topology image sample, ESPCN provides a sharper and higher contrast image over others methods as shown in Figure 4. By comparison, FSRCNN shows the highest PSNR value on the multi-material topology image sample, while ESPCN produces the highest value of SSIM as shown in Figure 5. The two IQA values indicate the higher image quality and the similarity between two images. However, in this study, the SR methods are used as the filter techniques in TO process. Moreover, the topology shapes are special types of image datasets. The low PSNR or SSIM values should not be interpreted to mean that those SR methods are not able to achieve good results. The TO process aims to minimize the objective function, which is the value of compliance. In this study, comparison of SR methods are investigated to find which one is more effective to the topology process than others.

4. Proposed method

4.1. Solid Isotropic Material with Penalization (SIMP) method

For density-based approach, SIMP is the most popular finite element-based TO method [67]. Material properties are uniformly distributed in the design domain, thus the densities in all finite elements become design variables [68]. Once the maximum structural stiffness is achieved, the minimum compliance C of the system can be obtained [69]. The objective function of C is as follows [70]:

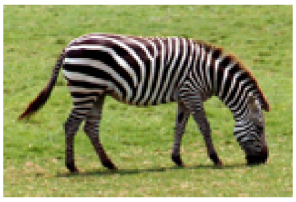

(a) Ground Truth (PSNR/SSIM)

(b) EDSR (32.42 dB/0.87)

(c) WDSR (32.51 dB/0.87)

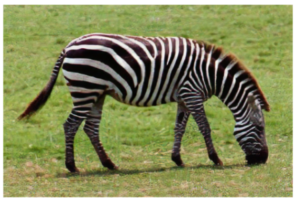

(d) SRGAN (29.73 dB/0.67)

(e) FSRCNN (34.23 dB/0.93)

(f) ESPCN (34.11 dB/0.94)

(g) LapSRN (34.06 dB/0.94)

Figure 3: $\times 4$ Super-resolution results for the "Zebra" example from **Set14** dataset using six super-resolution methods.

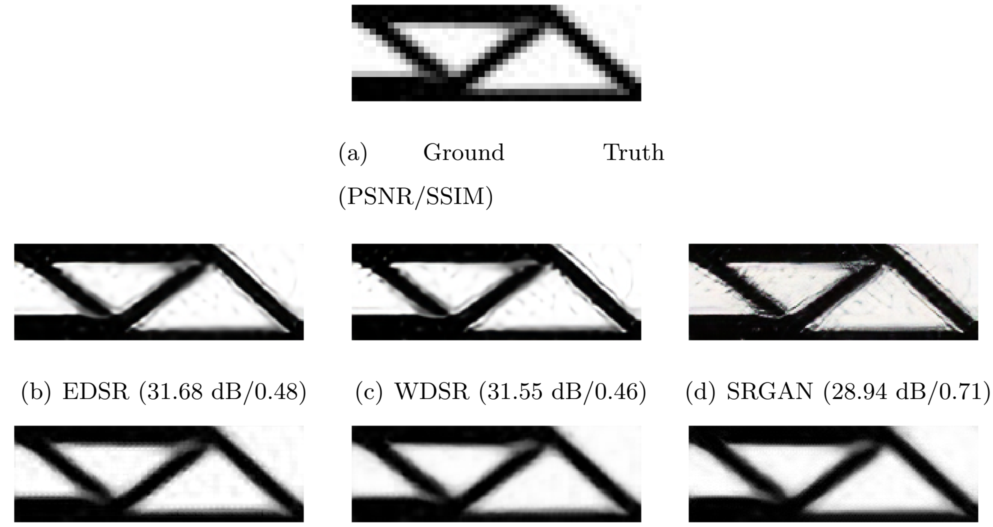

(a) Ground Truth (PSNR/SSIM)

(b) EDSR (31.68 dB/0.48) (c) WDSR (31.55 dB/0.46) (d) SRGAN (28.94 dB/0.71)

(e) FSRCNN (32.77 dB/0.56) (f) ESPCN (32.91 dB/0.94) (g) LapSRN (32.39 dB/0.63)

Figure 4: ×4 Super-resolution results for a single-material TO example using six super-resolution methods.

$$\left.\begin{array}{ll}\underset{\rho}{\text{Minimize}} & : C(\rho) = \dfrac{1}{2}\mathbf{U}^T\mathbf{K}\mathbf{U} \quad = \displaystyle\sum_{e=1}^{N}\frac{1}{2}(\mathbf{u}_e)^T\mathbf{k}_e\left(\rho_e\right)^p\mathbf{u}_e \\ \text{Subject to} & : \dfrac{\sum_{e=1}^{N} V_e\left(\rho_e\right)}{V_0} = V_f \\ & : \mathbf{K}\left(\rho_e\right)\mathbf{U} = \mathbf{F} \\ & : 0 < \rho_e \leq 1 \end{array}\right\} \tag{10}$$

where $\mathbf{k}_e$ and $\mathbf{K}\left(\rho_e\right)$ is the eth element and global stiffness matrix; $\mathbf{u}_e$, $\mathbf{U}$ indicate the eth element and global displacement and $\mathbf{F}$ is force vector, respectively. The ρ_e denoted the element density variable. $V(\rho_e)$ and V_0 in the volume constraints of the eth element and whole design domain, respectively; V_f is the volume constraint fraction. N, which is the number of elements, can be calculated as (nelx × nely). p is penalization parameter, which is usually set as 3 to force the intermediate design density variables to achieve either 0 (void) or 1 (solid) solutions.

In this paper, a density-based method [13, 14] is used as a basic filtering for the main process. Each element density is redefined as a weighted average of the densities before calling the finite element solver.

(a) Ground Truth (PSNR/SSIM)

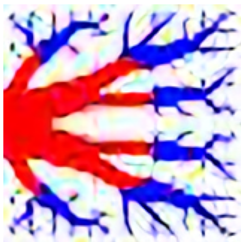

(b) EDSR (30.20 dB/0.32)

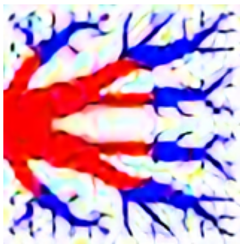

(c) WDSR (30.17 dB/0.33)

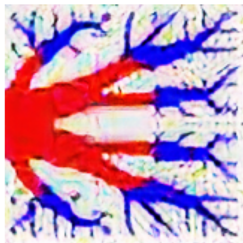

(d) SRGAN (28.64 dB/0.61)

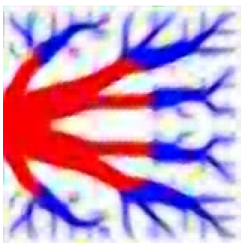

(e) FSRCNN (31.28 dB/0.55)

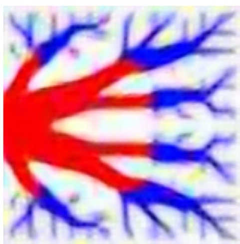

(f) ESPCN (30.92 dB/0.62)

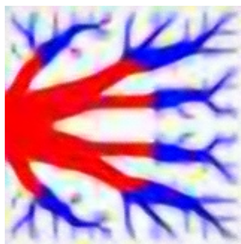

(g) LapSRN (30.71 dB/0.55)

Figure 5: ×4 Super-resolution results for a multi-material TO example using six super-resolution methods.

4.2. Optimality Criteria (OC)

OC is very popular in structural TO, in which minimum compliance is sought, subjected to a linear constraint on volume. It is an indirect method that first derives the stationary conditions at the optimum and then searches for the final design by applying recursive algorithms. Thus it is very efficient for problems with large number of design variables. Following a heuristic updating scheme [17] to update new solutions in optimization process can be formulated as:

$$\rho_e{}^{\text{new}} = \begin{cases} \max(\rho_{\min}, \rho_e - \varphi) \quad \text{if} \quad \rho_e B_e{}^{\eta} \leq \max(\rho_{\min}, \rho_e - \varphi) \\ \rho_e B_e{}^{\eta} \quad \text{if} \quad \max(\rho_{\min}, \rho_e - \varphi) < \rho_e B_e{}^{\eta} < \min(1, \rho_e + \varphi) \\ \min(1, \rho_e + \varphi) \quad \text{if} \quad \min(1, \rho_e + \varphi) \leq \rho_e B_e{}^{\eta} \end{cases} \tag{11}$$

where φ and η, which can vary from zero to one, are a positive move limit and numerical damping coefficient. Here, $\varphi = 0.2$ and $\eta = 0.5$, which are typical useful values [70], help to stabilize the iteration. B_e is obtained from the optimality condition as follows:

$$B_e = \frac{-\dfrac{\partial C}{\partial \rho_e}}{\lambda \dfrac{\partial V}{\partial \rho_e}} \tag{12}$$

where λ denotes the Lagrangian multiplier. The iterative process of OC algorithm is stopped when $(\left|\rho_e{}^{\text{new}} - \rho_e{}^{\text{old}}\right|)$ is smaller than a prescribed tolerance ϵ between two consecutive iterations. Otherwise, it will be continued until the convergence criterion is met.

4.3. Measure of discreteness

In order to measure the discreteness of design density variables in optimized designs, Sigmund [9] proposed a indicator $M(\%)$ as follows:

$$M(\%) = \frac{\sum_{e=1}^{N} 4\rho_e \left(1 - \rho_e\right)}{N} \times 100\% \tag{13}$$

If there are no regions with intermediate design variable values, $M = 0$ (%). When the final design is totally grey, $M = 100(\%)$. It should be noted that all parameters and calculations are assumed to be non-dimensional, unless otherwise specified.

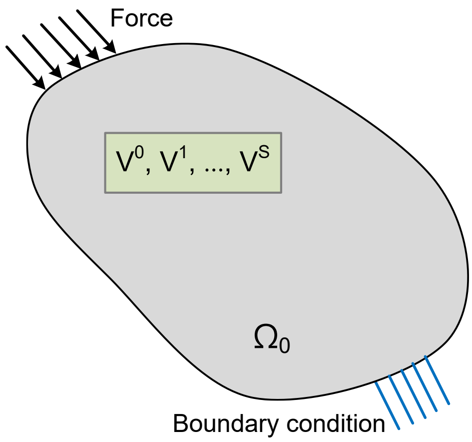

Figure 6: Schematic diagram of the multi-material TO design.

4.4. Multi-material topology optimization

Consider the multi-material problem illustrated in Figure 5. The aim is to search the optimal distribution of different types of materials with a given design domain Ω_0. Here, a set of $S+1$ materials including void is specified and the compliance must be minimized under subject to a total mass constraint. The relative density of material i is $\rho_e^i \in (0,1)$ at an element e. The sum of the density of all phases at any arbitrary points $\mathbf{x} = \{x, y\}$ within the design domain Ω must conform to the following constraint [11]

$$\sum_{i=0}^{S} \rho^i = 1 \tag{14}$$

Thus, the multi-material problems using the SIMP method can be expressed by:

$$\left.\begin{aligned}
&\underset{\rho}{\text{Minimize}} && : C(\rho) = \frac{1}{2}\mathbf{U}^T\mathbf{K}\mathbf{U} \\
&\text{Subject to} && : \frac{\sum_{i=0}^{S}\sum_{e=1}^{N} V_e^i\left(\rho_e^i\right)}{V_0} = V_f \\
& && : \mathbf{K}\left(\rho_e\right)\mathbf{U} = \mathbf{F} \\
& && : 0 < \rho_e \leq 1
\end{aligned}\right\} \tag{15}$$

where $\rho = \left\{\rho^1, \cdots, \rho^i, \cdots, \rho^S\right\}$ stands for the density vector including all phases, in which $\rho^i = \left\{\rho_1^i, \cdots, \rho_e^i, \cdots, \rho_N^i\right\}$ is the vector of all element density of the i^{th} phase, and ρ_e^i is the e^{th} element analysis density with respect to the i^{th} phase. The density constraints in Eq. (14) lead the following equation to be satisfied naturally,

$$\sum_{i=0}^{S} V_e^i = \int_{\Omega_e} \mathrm{d}\Omega_e \tag{16}$$

4.5. Alternating active-phase algorithm for multi-material

The purpose of the alternating active-phase algorithm is to divide a multi-phase problem into several single-material sub-problems with only one constraint [71]. The algorithm has an outer iteration in which a total number of $S(S-1)/2$ sub-problems are solved partially. A sequential chain of different material phases is partially performed using a binary phase based-TO method. During the process of every sub-problem, the topologies of $S-2$ phases are fixed and only two active phases are considered to update. If the two active phases are denoted by a and b, the density values of each phase could be altered in a single loop and their relationship must satisfy the following condition:

$$\rho^a + \rho^b = 1 - \sum_{i=1, i\neq(a,b)}^{S} \rho^i \tag{17}$$

For binary phase sub-problem, the only density values of phase a are considered as design variables. After attaining ρ^a, the density value of phase b can be computed by

$$\rho^b = \sum_{j=a,b} \rho^j - \rho^a \tag{18}$$

It is clear from Eq. (17) that the corresponding upper bound for both phases a and b has been replaced 1 with $\sum_{j=a,b} \rho^j$ while the lower bound is fixed as $1 < \rho^{a,b,min} < \rho^{a,b} < \sum_{j=a,b} \rho^j$.

4.6. Multi-material interpolation scheme

A large number of interpolation schemes for the multi-material problems has been introduced. Young's modulus and density variables of the material phases are proposed using a penalization parameter. In this study, Zhou and Wang's [72] multi-material interpolation scheme is adopted. The methods can obtain partial material properties from the set of input material data. Its explicit mathematical expression for the eth element is given as

$$E\left(\rho_e^i\right)=\sum_{i=1}^{S}\left(\rho_e^i\right)^p E^i \tag{19}$$

where E^i is the Young's modulus of the i$^t h$ material phase ($i = 1, 2, \cdots, S$), and p indicates the penalization parameter, which is is usually set as 3 to impose the intermediate density variables approaching either 0 (void) and 1 (solid).

4.7. Super-resolution topology optimization (SRTO) method

The proposed method, namely, SRTO, which is provided in Algorithm 1, uses the trained SR image reconstruction methods. The trained SR is added to the inner loops to reconstruct the topology images. In the main iteration, the element densities are computed using the typical TO method mentioned above. However, the trained SR networks are used to obtain HR images from the LR images at the end of each iteration. After finishing the reconstruction process, the main TO method recovers the original size images from the HR images for the next iteration. Figure 7 shows the flowchart of the proposed method using trained SR network in inner loop. In the typical TO process, LR images are fed into the SIMP and OC methods. After updating the LR image, the updated design variables are reconstructed using the trained SR methods at each iteration. The obtained $\times 4$ SR results are then resized back to the original discretized size for the next iteration. The trained SR methods are used as filter techniques to enhance the topology images. The grey transition regions can be removed using the trained SR methods and compliance values are improved. After termination, the final LR image can be converted into $\times 4$ HR one using the trained SR methods. In the next section, the results obtained from the proposed model will be compared with those of the typical TO process.

Algorithm 1: SRTO

Input: Domain, nelx, nely, V_f (prescribed volume fraction), E (Young's modulus), ν (Poisson ratio)

Output: Optimized structural topology

```
do
    for each e to N do
        Compute compliance by using FEA: Σ_{e=1}^{N} 1/2 (u_e)^T k_e (ρ_e)^p u_e
        Sensitivity anlaysis
        Density-based filtering
        Update ρ using OC method
        Upscale resolution using SR method
        Downscale resolution for the next step
        Replace ρ by the new image from the previous step
        Constraints: (Σ_{e=1}^{N} V_e(ρ_e)) / V_0 = V_f, K(ρ_e) U = F, 0 < ρ_e ≤ 1
    end
while Any of the stopping criteria is satisfied
return
```

Compute compliance by using FEA: $\sum_{e=1}^{N} \frac{1}{2} (\mathbf{u}_e)^T \mathbf{k}_e (\rho_e)^p \mathbf{u}_e$

Constraints: $\dfrac{\sum_{e=1}^{N} V_e(\rho_e)}{V_0} = V_f$, $\mathbf{K}(\rho_e)\,\mathbf{U} = \mathbf{F}$, $0 < \rho_e \leq 1$

5. Numerical examples

In this section, various benchmark TO problems for both single and multiple-materials are performed to illustrate the effectiveness of the proposed SRTO methods. A scale factor of $\times 4$ between LR and HR images is used. The maximum allowed iteration number is defined as 50 and the parameter penalization of 3 is used. The trained SR methods are used to reconstruct the LR topology shapes to SR images at each iteration. The LR image at every generation is fed into the trained SR methods; the SR methods then gave the reconstructed image back for the next generation. Moreover, the proposed methods use the SR image reconstruction strategy as post-process tools to refine the LR image into HR results at the end of the last iteration. All final topologies are taken from the 50^{th} iteration step. The pre-trained networks and weights of

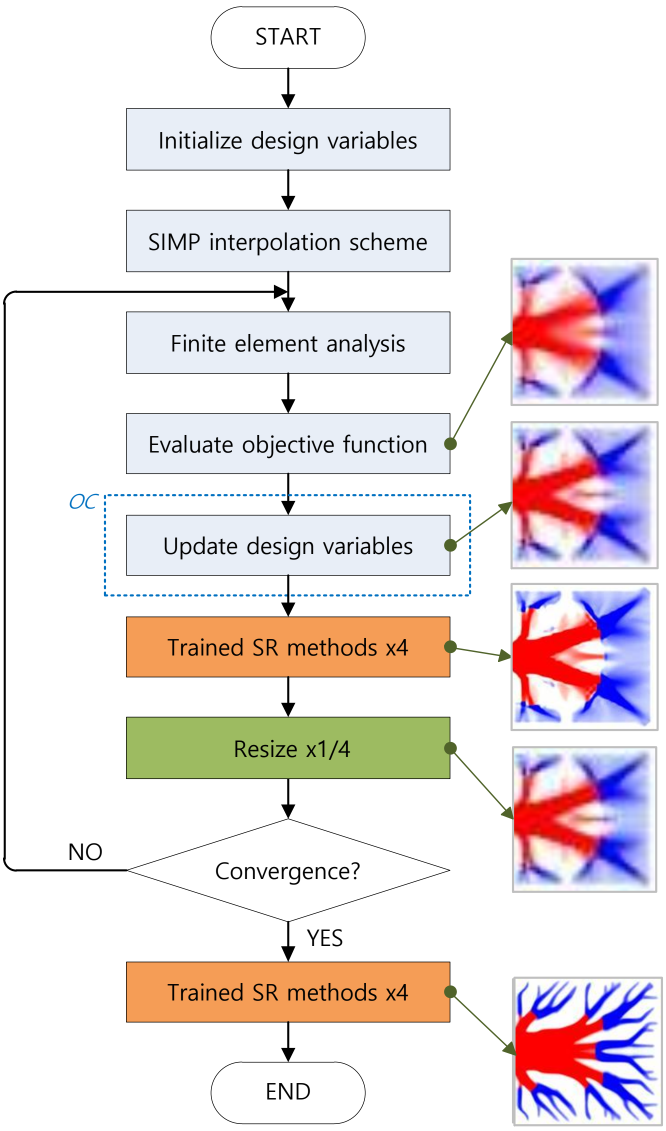

Figure 7: Flowchart of the proposed method using trained SR networks in inner loop.

326 EDSR[1], WDSR[2], and SRGAN[3] are obtained from online material supplementaries[4] and those for
327 FSRCNN[5], ESPCN[6], and LapSRN[7] from GitHub. All early-stage SIMP results are compared with

[1]https://github.com/LimBee/NTIRE2017
[2]https://github.com/JiahuiYu/wdsr ntire2018
[3]https://github.com/david-gpu/srez
[4]https://github.com/krasserm/super-resolution
[5]https://github.com/Saafke/FSRCNN_Tensorflow/tree/master/models
[6]https://github.com/fannymonori/TF-ESPCN
[7]https://github.com/fannymonori/TF-LapSRN/tree/master/export

those obtained by the proposed method at the same resolution. After the iteration is terminated (Figure 7), the final topologies can be obtained with $\times 4$ resolution. The problems are solved for various discretizations, sensitivity filtering radius R and specific conditions.

5.1. Single-material examples

Three examples as shown in Figure 8 including MBB beam [73] and L-shaped beam [74] with rectangular finite elements discretization as well as curved beam, which is discretized to form a grid in polar coordinates, are considered. The goal is to minimize the compliance of these beams subjected to a volume fraction constraint and other conditions. The Young's modulus, Poisson's ratio and thickness of the beam are $E = 1.0$, $\nu = 0.3$ and 1, respectively. The volume fraction constraint is chosen to be 0.5. The sensitivity filtering radius $R = 2$ for MBB beam and $R = 1.5$ for L-shaped and curved beam.

5.1.1. MBB beam

Due to symmetry, only half design domain of simply-supported MBB beam under concentrated load P $= 1$ which has a length-to-height ratio, $3:1$ with $L = 20$ (Figure 8(a)) is analysed. It is discretized with 48×16 bi-linear quadrilaterals for the iteration of the SRTO methods. Figure 9(a) shows the compliance convergence history using the SIMP and six SRTO methods. They converge rapidly within $20-30$ iterations and become steadily afterwards. The typical SIMP method reaches its optimum faster than the SRTO ones. However, the optimum values of SRTO-edsr and -wdsr are lower than those of SIMP. Their effectiveness can be compared with the values of compliance and measure of discreteness presented in Table 1. The proposed SRTO method using WDSR shows the lowest values of compliance and measure of discreteness.

The topology images of several iteration steps can be identified via the compliance convergence history in Figure 10(a) and the final ones obtained by all methods are shown in Figure 11. The SRTO-srgan tends to produce grey blur parts on the white void region, while the result of SRTO-wdsr has higher contrast image. Moreover, those of SRTO-fsrcnn, SRTO-espcn, and SRTO-lapsrn also have less sharper and lower contrast images. The disadvantage makes the C and M values be higher than those of SRTO-wdsr. It is clear from Figure 11 that the proposed SRTO methods can enhance the topology resolution and the WDSR is suitable for the MBB topology example. However, because the double lines still remain near boundaries, another post-processing is needed to remove the transition regions.

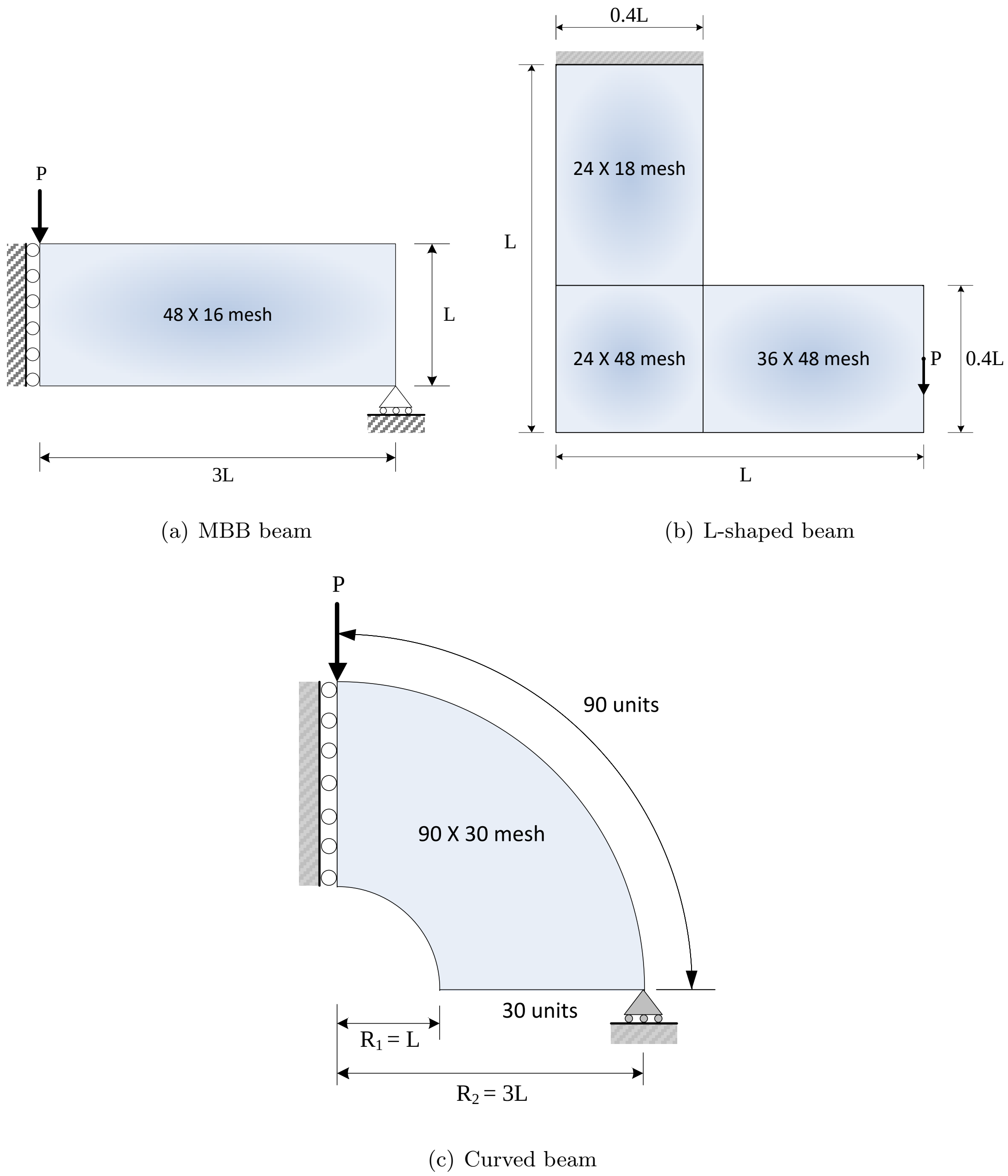

Figure 8: Geometry, boundary conditions, and applied load in the design domain of single-material examples.

Table 1: The compliance and measure of discreteness for single-material examples with $V_f = 0.5$ at the 50th iteration.

Method	SIMP	SRTO-edsr	SRTO-wdsr	SRTO-srgan	SRTO-frcnn	SRTO-espcn	SRTO-lapsrn
MBB beam							
C*	210.987	208.518	205.925	219.546	216.973	217.385	221.171
M†	21.889	20.818	20.818	34.926	28.186	28.867	30.131
L-shaped beam							
C*	192.932	193.028	192.296	197.548	193.788	194.015	194.437
M†	31.589	33.382	32.616	41.448	34.581	34.227	34.687
Curved beam							
C*	56.369	56.463	56.287	58.951	56.694	56.802	57.076
M†	32.913	34.729	34.511	44.367	35.872	35.156	36.110

* Compliance.

† Measure of discreteness.

5.1.2. L-shaped cantilever beam

A L-shaped cantilever beam with L=30 and three different discretization is subjected to a concentrated load P = 1 at the middle of right free edge as shown in Figure 8(b). After the 30^{th} iteration, only SRTO-wdsr shows lower optimum compliance values compared to those of typical SIMP (Figure 9(b)). The optimum compliance of SRTO-wdsr from Table 1 is 192.296 while that of typical SIMP is 192.932. Similar to the MBB beam problem, the SRTO-srgan and SRTO-lapsrn could not achieve good results compared to other methods. Compliance convergence history using SRTO-wdsr is shown in Figure 10(b). In Figure 12, the zoomed images of final topologies obtained by all methods can be investigated in details. Except from SRTO-wdsr, the results of other SRTO methods does not produce clear-cut outline along the contour of the topologies. The grey blur parts tend to broad uncertain black region to the white void region when HR image is resized and fed into the topology process back.

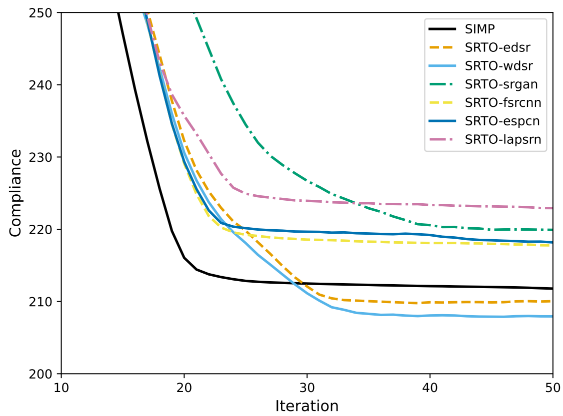

(a) MBB beam

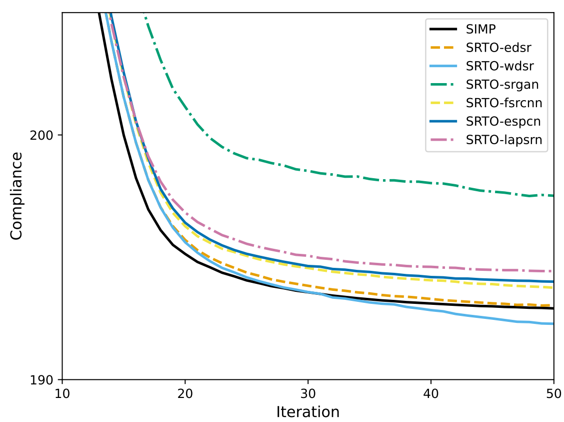

(b) L-shaped beam

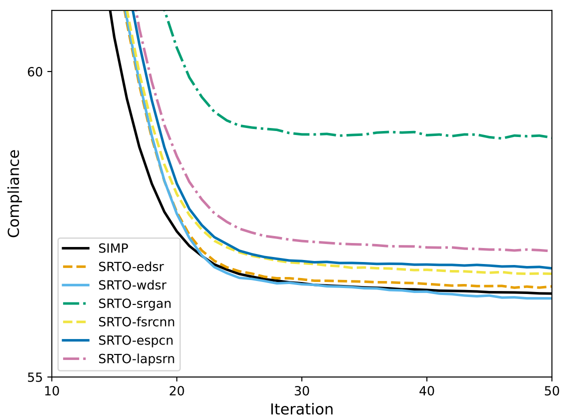

(c) Curved beam

Figure 9: Compliance convergence history of single-material examples using various methods.

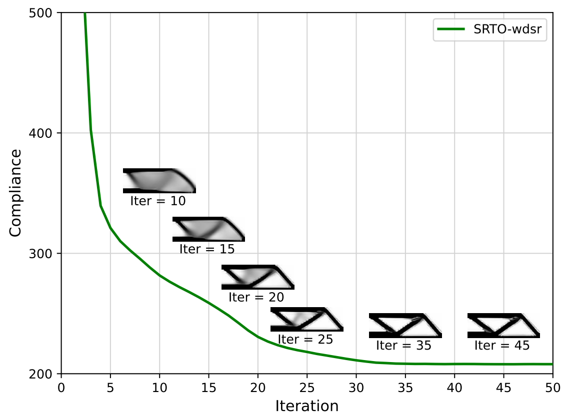

(a) MBB beam

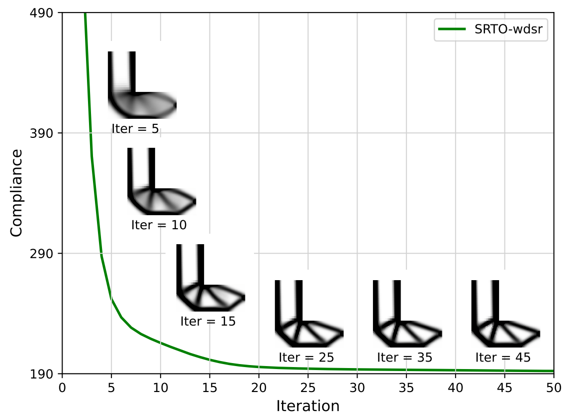

(b) L-shaped beam

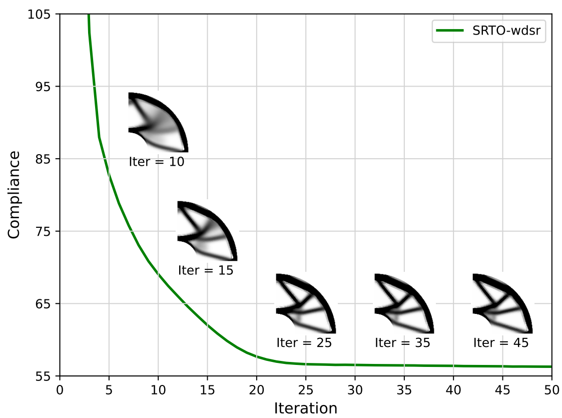

(c) Curved beam

Figure 10: Compliance convergence history of single-material examples using SRTO-wdsr.

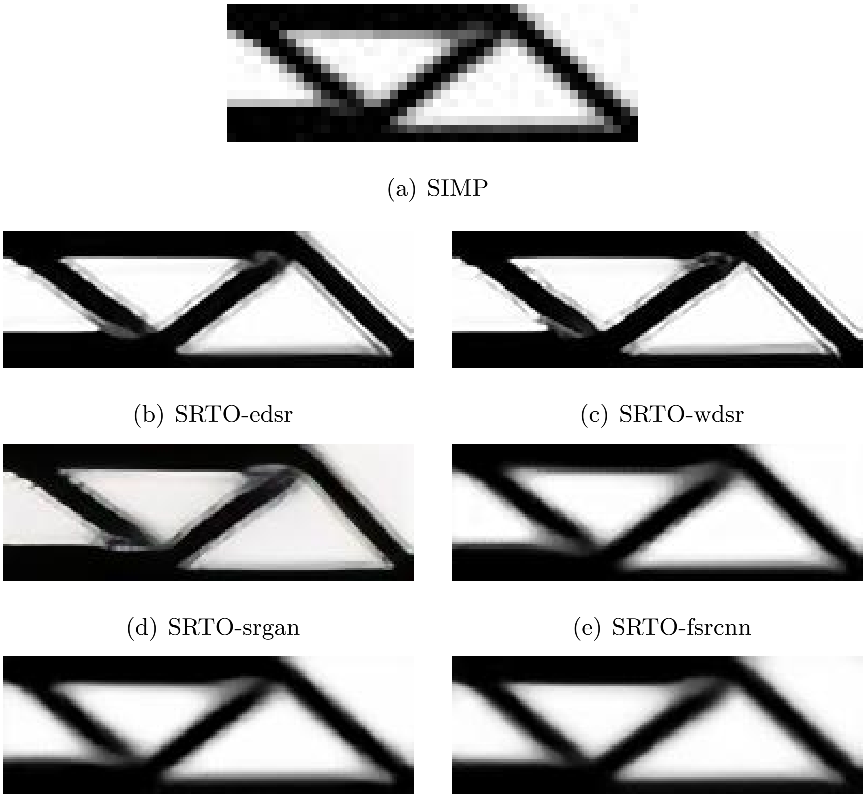

(a) SIMP

(b) SRTO-edsr

(c) SRTO-wdsr

(d) SRTO-srgan

(e) SRTO-fsrcnn

(f) SRTO-espcn

(g) SRTO-lapsrn

Figure 11: The final topologies of the MBB beam obtained by various methods in which SRTO-wdsr has the minimum compliance.

5.1.3. Curved beam

The geometric descriptions and boundary conditions of curved beam with $R_1 = L = 10$ and $R_2 = 30$ are shown in Figure 8(c). It is under a concentrated force $P = 1$ on its top-left corner. Figure 9(c) shows the compliance convergence history using all methods. After the 20^{th} iteration, the SRTO-wdsr shows lower optimum compliance values compared to those of typical SIMP method, which is also verified in Table 1. SRTO-wdsr produces the lowest compliance, however discreteness is higher than those of the SIMP method. Compliance convergence history using SRTO-wdsr and the topology images of five iteration steps are plotted in Figure 10(c). The zoomed images of final topologies obtained by all SRTO methods taken from 50^{th} iteration step are shown in Figure 13.

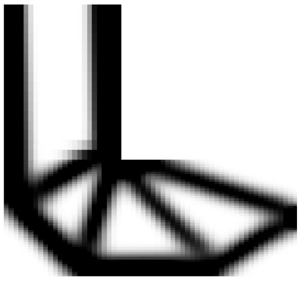

(a) SIMP

(b) SRTO-edsr

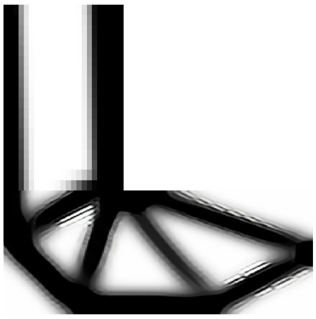

(c) SRTO-wdsr

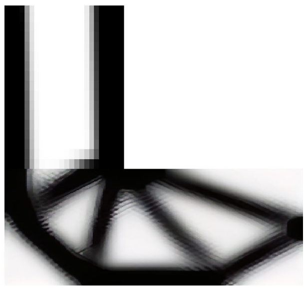

(d) SRTO-srgan

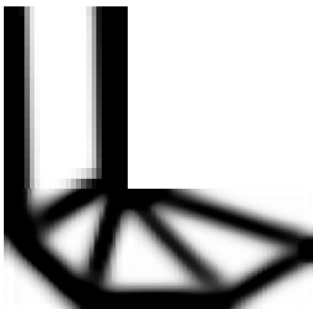

(e) SRTO-fsrcnn

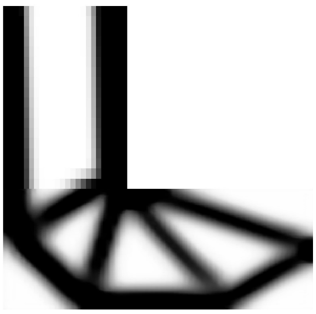

(f) SRTO-espcn

(g) SRTO-lapsrn

Figure 12: The final topologies of the L-shaped cantilever beam obtained by various methods in which SRTO-wdsr has the minimum compliance.

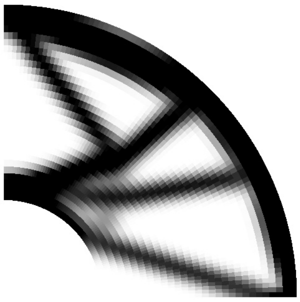

(a) SIMP

(b) SRTO-edsr

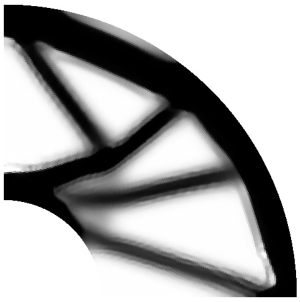

(c) SRTO-wdsr

(d) SRTO-srgan

(e) SRTO-fsrcnn

(f) SRTO-espcn

(g) SRTO-lapsrn

Figure 13: The final topologies of the curved beam obtained by various methods in which SRTO-wdsr method has the minimum compliance.

Table 2: Material properties and volume fraction constraints for multi-material examples.

Test problem	Material	Color	E†	V_e*
Compliant inverter	1		2	0.1
	2		1	0.2
	0(void)		10^{-9}	0.7
Compliant gripper	1		2	0.1
	2		1	0.2
	0(void)		10^{-9}	0.7
Heat	1		2	0.2
	2		1	0.2
	0(void)		10^{-9}	0.6

* Volume fraction constraint of each material.

† None scale.

5.2. Multi-materials examples

In order to verify the effectiveness of the proposed methods further, three examples of multi-materials as shown in Figure 14 including displacement inverter mechanism, compliant gripper mechanism and heat conduction are considered. For displacement inverter and compliant gripper mechanism, since the design domain is symmetric from top to bottom, its bottom half is used to reduce the computational cost. Unlike with previous single-material examples, because these multi-material examples use two colors as shown in Table 2, the ×4 SR results tend to distort the LR image in the early design stage. For this reason, the topology images are constructed by using the SIMP method until the 10 iterations, and then the SRTO methods are used to enhance them. The Young's modulus of the phases, volume fraction constraints are provided in Table 2 and Poisson's ratio of 0.3 and thickness of 1 are used. The sensitivity filtering radius $R = 1.2$ for displacement inverter mechanism, compliant gripper mechanism and $R = 1.12$ for heat conduction.

5.2.1. Displacement inverter mechanism

The bottom half of the design domain and boundary conditions of the displacement inverter mechanism with L= 40 is provided in Figure 14(b). An input force $F_{in} = 1$ is applied at the center of the left edge. It is discretized using a mesh of $n_x \times n_y = 40 \times 20$ elements. The objective is to maximize the output displacement $U_{x,out}$ at point A. It is from Figure 15(a) that all results obtained by six SRTO methods show unstable pattern within $11 - 40$ iterations. In particular, the results of the SRTO-fsrcnn and SRTO-lapsrn can not converge below that of SIMP method. The unexpected blue lines (SRTO-espcn) lead to the higher convergence. Only result of the SRTO-wdsr shows the stable convergence history. The displacement convergence history obtained using SRTO-wdsr is shown in Figure 16(a) with the six topology images at corresponding iteration steps. Figure 17 shows the final topologies of all methods. The results obtained from the SRTO-fsrcnn and SRTO-lapsrn give different topologies as compared to those of other methods. Moreover, the topology results of the SRTO-edsr, SRTO-srgan, and SRTO-espcn obtain distorted connection parts (blue color). In contrast, the SRTO-wdsr can improve topology image as shown in Figure 17(c).

5.2.2. Compliant gripper mechanism

The design domain and boundary conditions of compliant gripper mechanism are given in Figure 14(d). Both top and bottom corners on the left edge are fixed, and the input force $F_{in} = 1$N is loaded at the midpoint of the left side with the input spring with stiffness $k_{in} = 0.1$. The objective of the compliant mechanism gripper is to obtain the optimized topology design so that the mechanism can lead to the expected output displacement $U_{y,out}$ with constant output spring with stiffness $k_{out} = 0.1$. The objective is to maximize the output displacement $U_{y,out}$ at point A. Figure 15(b) shows the displacement convergence history obtained using the six SRTO methods. Compared with the result of SIMP, the only one of the SRTO-wdsr is higher, while the rest are the lower. The convergence history of the SRTO-wdsr with six topologies of arbitrary iteration steps is shown in Figure 16(b). The final topologies are given in Figure 18. The five topology images obtained by SRTO-edsr, -srgan, -fsrcnn, -espcn, and -lapsrn exhibit blurry outline along the contour. In particular, the SRTO-srgan tends to make the ivory-coloured background. The

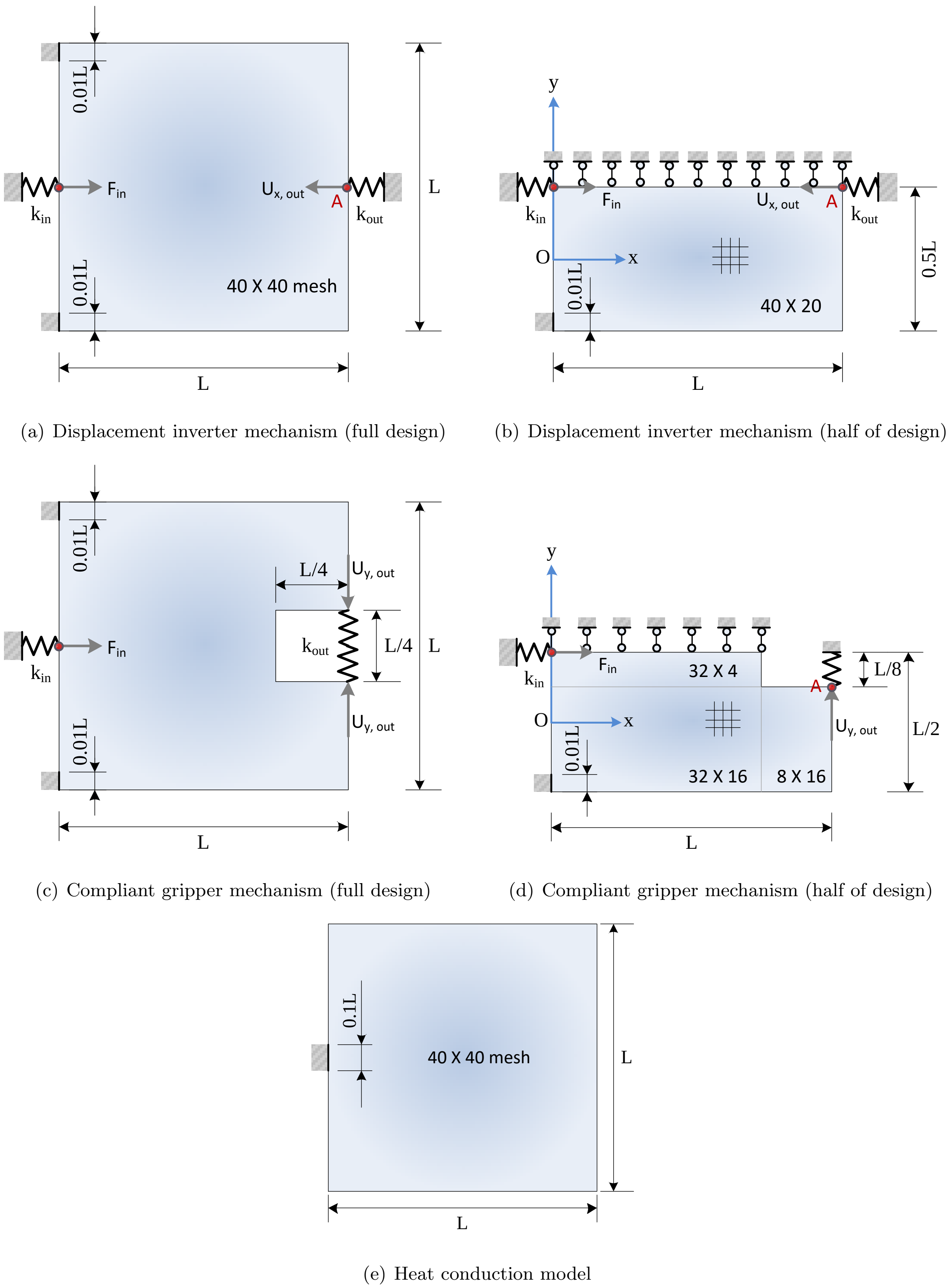

(a) Displacement inverter mechanism (full design)
(b) Displacement inverter mechanism (half of design)
(c) Compliant gripper mechanism (full design)
(d) Compliant gripper mechanism (half of design)
(e) Heat conduction model

Figure 14: Design domain and boundary conditions of the displacement inverter mechanism, compliant gripper mechanism and heat conduction.

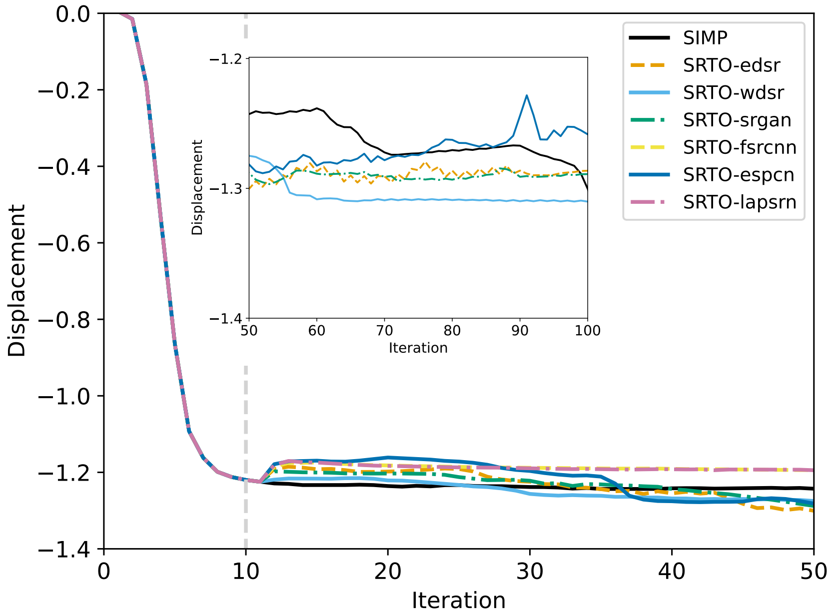

(a) Displacement inverter mechanism

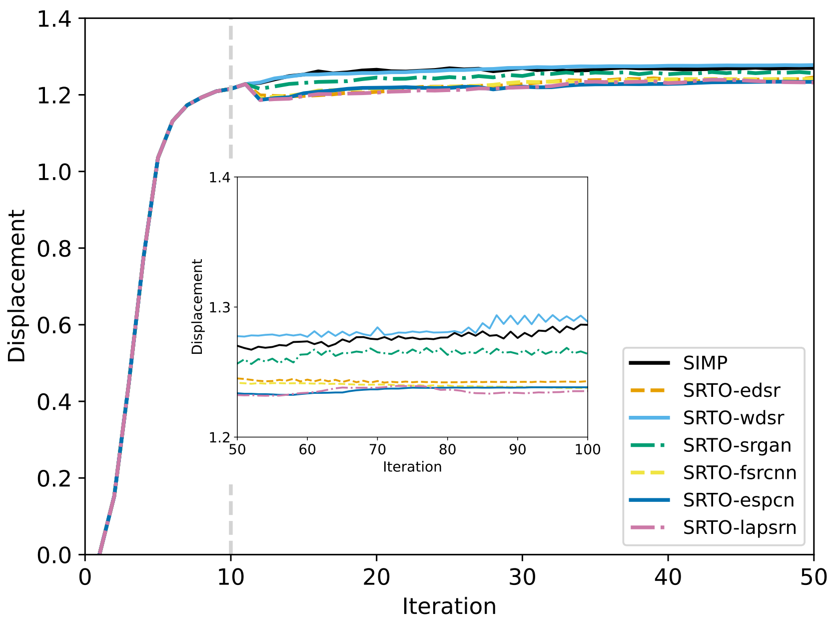

(b) Compliant gripper mechanism

Figure 15: Convergence history of the displacement inverter mechanism and compliant gripper mechanism obtained using various methods.

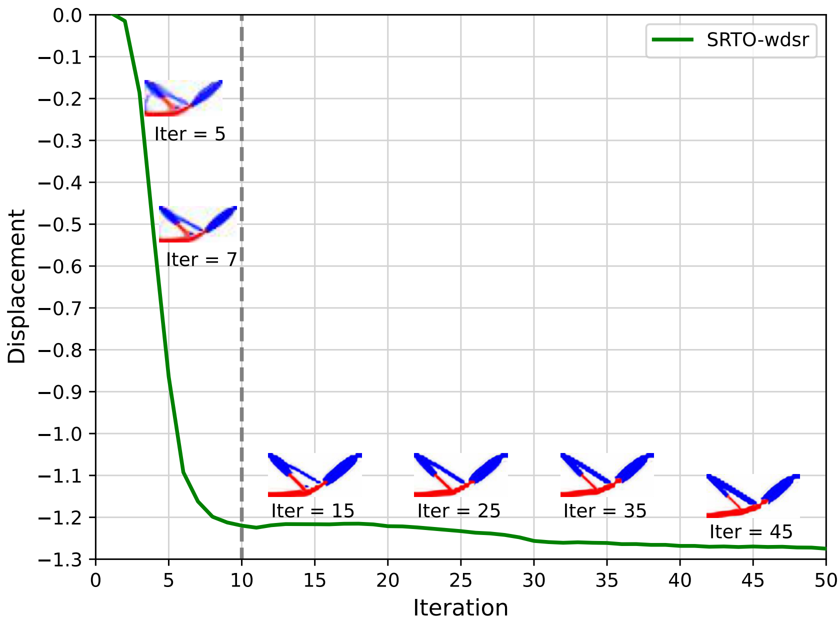

(a) Displacement inverter

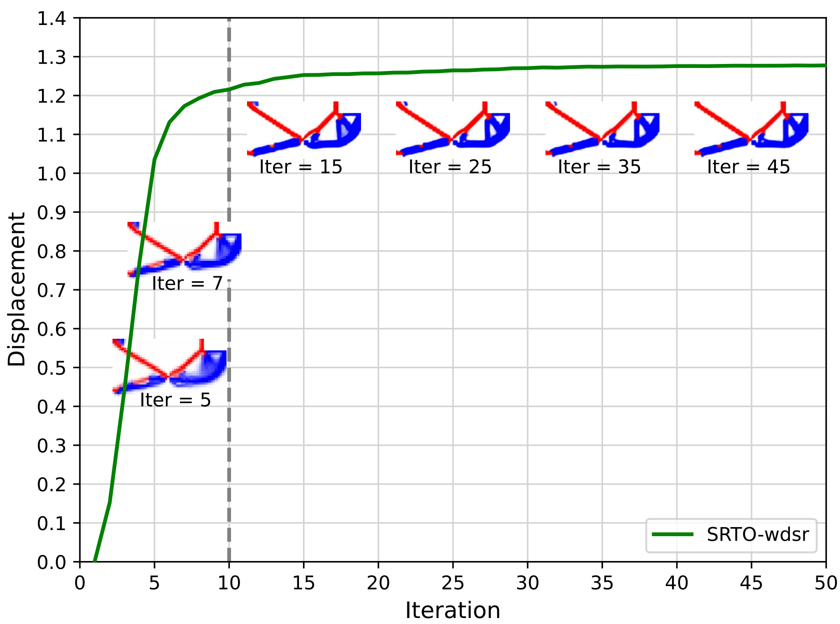

(b) Displacement gripper

Figure 16: Convergence history of the displacement inverter mechanism and compliant gripper mechanism using SRTO-wdsr.

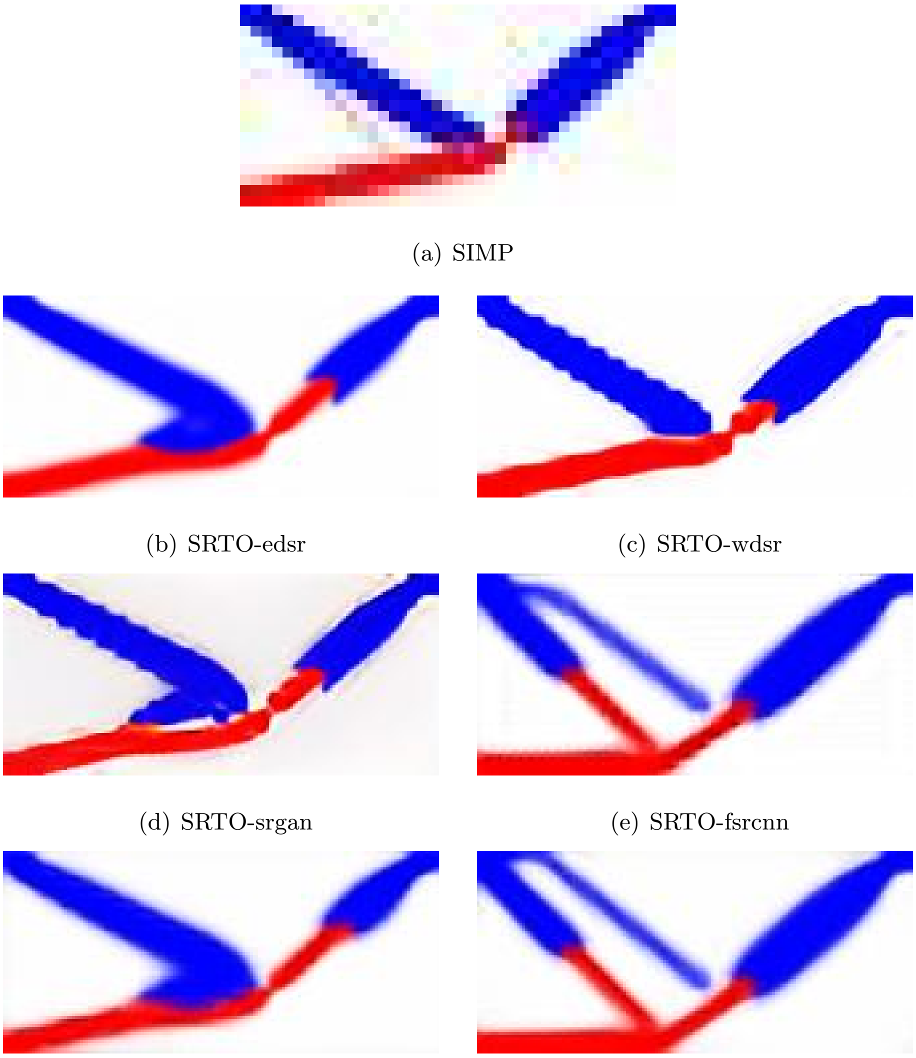

(a) SIMP

(b) SRTO-edsr

(c) SRTO-wdsr

(d) SRTO-srgan

(e) SRTO-fsrcnn

(f) SRTO-espcn

(g) SRTO-lapsrn

Figure 17: The final topologies of the displacement inverter mechanism obtained by various methods in which the result of SRTO-wdsr has the absolute maximum displacement.

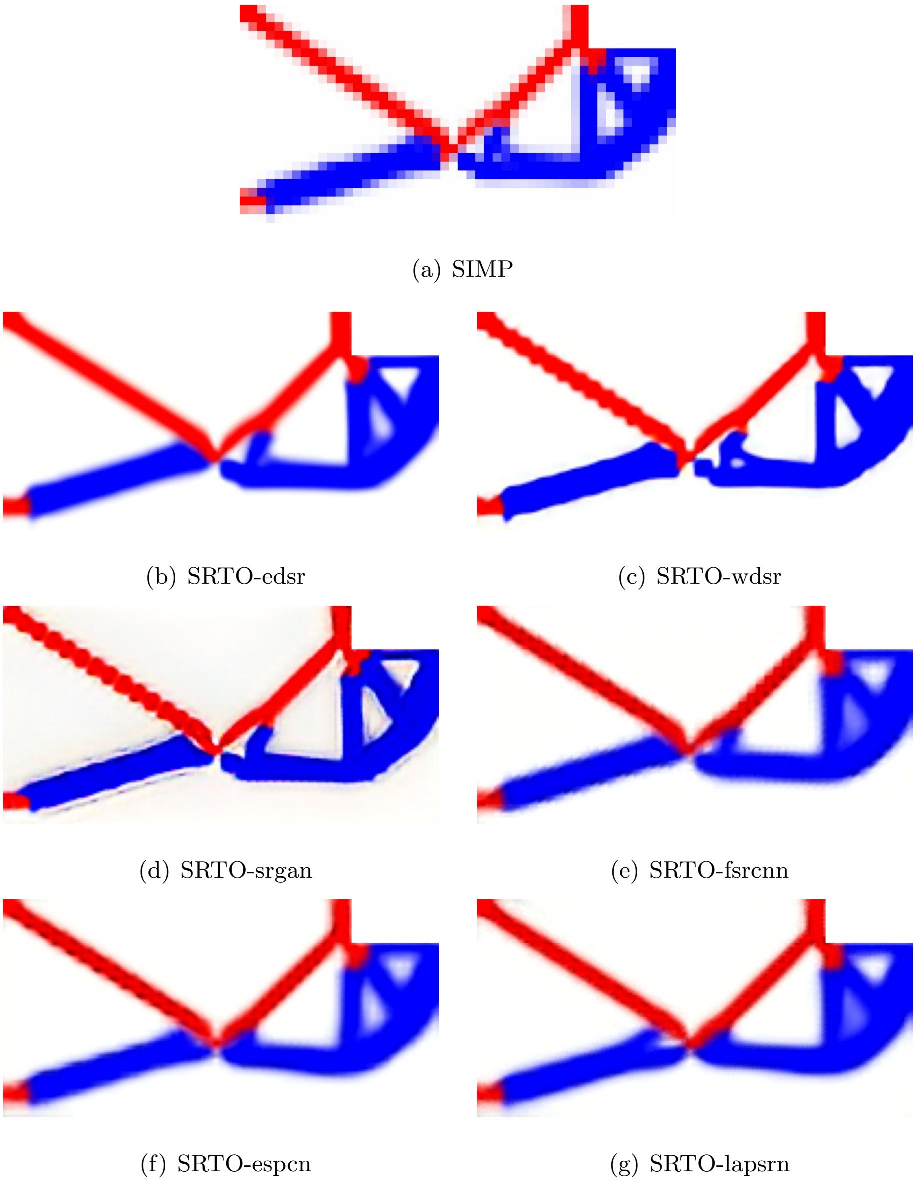

Figure 18: The final topologies of the compliant gripper mechanism obtained by various methods in which the result of SRTO-wdsr has the maximum value of displacement.

topology result of the SRTO-wdsr is a much sharper and higher contrast images.

5.2.3. Heat conduction problem

The design domain and boundary conditions of 2D heat conduction model are provided in Figure 14(e). At nodes, heat flow is conducted into the system. The heat conductivity coefficient $k_x = k_y = 1$ and internal heat supply $Q = 1$ is assumed to be uniformly distributed over model. The objective is to minimize the compliance computed by the formula $c = 1/2\mathbf{T}^T\mathbf{F}$ thus the optimized model can have the optimal thermal conductivity. The compliance convergence history is shown in Figure 19(a). It is clear that the result obtained using SRTO-edsr shows the minimum curve. The result of SRTO-fsrcnn also has lower convergence history line compared to that of SIMP method. The convergence history of the SRTO-edsr with six topologies of arbitrary iteration steps is shown in Figure 19(b). It can be seen that all topology images are different from each other and those of SRTO-fsrcnn, -espcn, and -lapsrn show blurry images. However, the final topology of SRTO-edsr gives a much higher contrast image compared to others as shown in Figure 20.

6. Conclusion

This study proposes a new topology optimization method to enhance the topology images using six different super-resolution methods, namely, EDSR, WDSR, SRGAN, FSRCNN, ESPCN, and LapSRN. The trained SR methods are added to the inner loops of the TO process to upscale from the course mesh topology to High-Resolution image ($\times 4$). Six well-known single- and multi-material TO examples are examined to demonstrate the effectiveness of the proposed method. The SRTO-wdsr achieves the good results in all cases except for the heat conduction problem, in which the SRTO-edsr obtains the best one. Their final topologies provide noticeably improvement over those of typical SIMP method and create a much sharper and higher contrast images. Moreover, the proposed TO strategy using the super-resolution image reconstruction methods can give valuable innovation for conventional TO process.

7. Limitations and future work

The proposed procedure seems particularly effective when the original mesh is quite coarse and requires high computation cost. There are some limitations associated with the application

, Thuc P. Vo, Joowon Kang, Jaehong Lee, Topology optimization using super-resolution image reconstruction methods, Advances in Engineering Software, Volume 177, 2023, 103413, ISSN 09

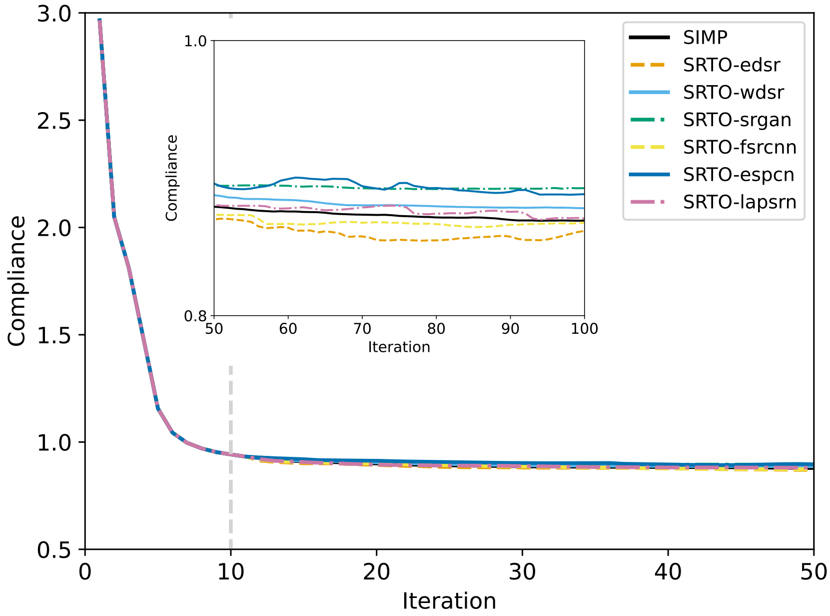

(a) Various methods

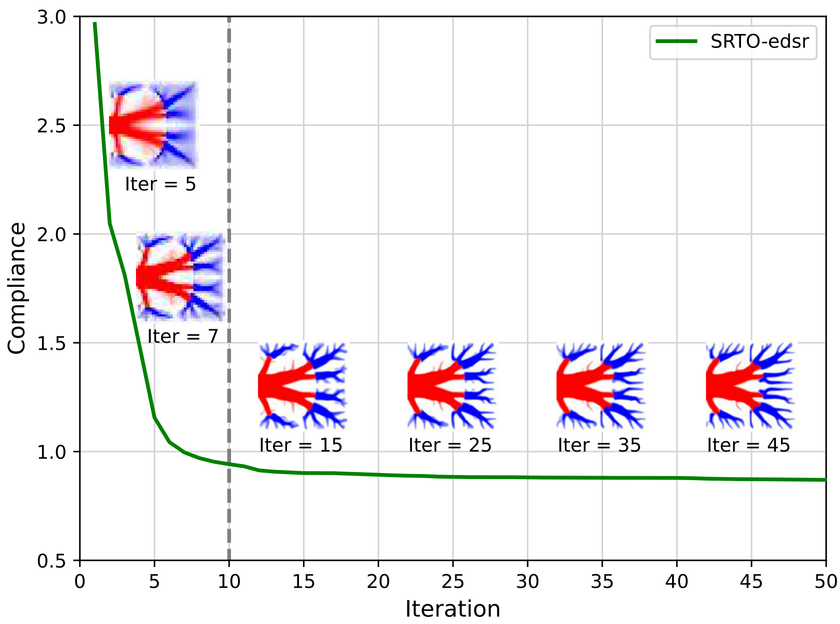

(b) SRTO-edsr method

Figure 19: Compliance convergence history of the heat conduction model obtained using various methods.

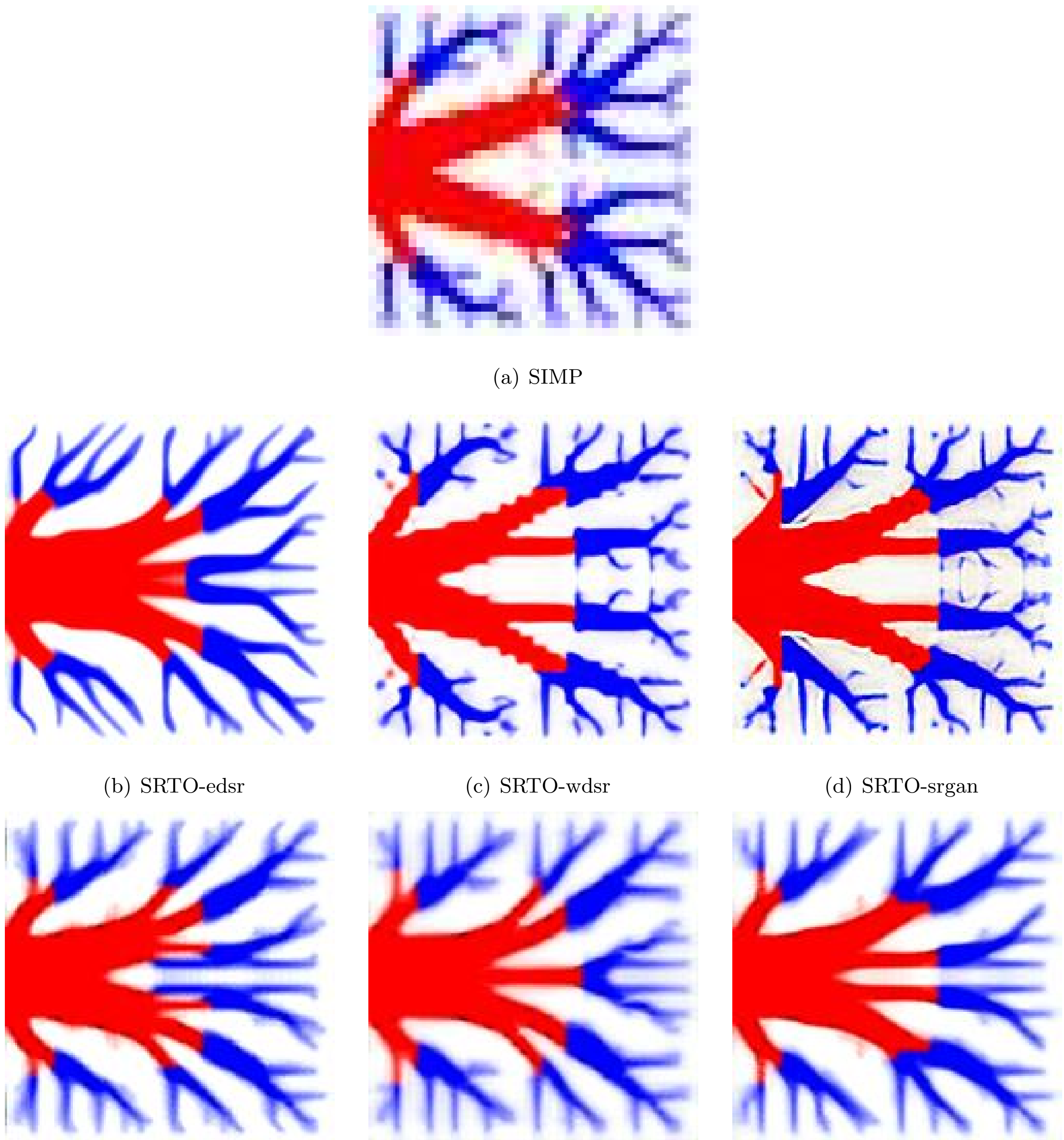

(a) SIMP

(b) SRTO-edsr

(c) SRTO-wdsr

(d) SRTO-srgan

(e) SRTO-fsrcnn

(f) SRTO-espcn

(g) SRTO-lapsrn

Figure 20: The final topologies of the heat conduction model obtained by various methods in which the result of SRTO-edsr has the minimum value of displacement.

of proposed method to the original TO process directly, due primarily to the characteristics of the method in which the SR step does not adjust the sensitivity analysis or the OC process. Furthermore, if the filter size does not meet special constraints, then the obtained solutions might not be applicable to the practical problems. The next topic can be a direct method to adjust the sensitivity filter or the objective function by using the resolution colour value from the SR methods.

Acknowledgement

This research was supported by a grant (NRF-2020R1A4A2002855) from NRF (National Research Foundation of Korea) funded by MEST (Ministry of Education and Science Technology) of Korean government.

References

[1] M. P. Bendsøe, O. Sigmund, Topology optimization: theory, methods, and applications, Springer Science & Business Media, 2003.

[2] C.-Y. Wu, K.-Y. Tseng, Topology optimization of structure using differential evolution, J. Syst. Cybern. Inform 6 (1) (2008) 46–51.

[3] A. G. M. Michell, LVIII. The limits of economy of material in frame-structures, The London, Edinburgh, and Dublin Philosophical Magazine and Journal of Science 8 (47) (1904) 589–597. doi:10.1080/14786440409463229.

[4] O. Sigmund, K. Maute, Topology optimization approaches, Structural and Multidisciplinary Optimization 48 (6) (2013) 1031–1055. doi:10.1007/s00158-013-0978-6.

[5] G. I. N. Rozvany, W. Prager, Optimal design of partially discretized grillages, Journal of the Mechanics and Physics of Solids 24 (2-3) (1976) 125–136. doi:10.1016/0022-5096(76)90022-3.

[6] M. P. Bendsøe, N. Kikuchi, Generating optimal topologies in structural design using a homogenization method, Computer Methods in Applied Mechanics and Engineering 71 (2) (1988) 197–224. doi:10.1016/0045-7825(88)90086-2.

[7] G. I. N. Rozvany, A critical review of established methods of structural topology optimization, Structural and Multidisciplinary Optimization 37 (3) (2008) 217–237. doi:10.1007/s00158-007-0217-0.

[8] M. P. Bendsøe, Optimal shape design as a material distribution problem, Structural Optimization 1 (4) (1989) 193–202. doi:10.1007/bf01650949.

[9] O. Sigmund, Morphology-based black and white filters for topology optimization, Structural and Multidisciplinary Optimization 33 (4-5) (2007) 401–424. doi:10.1007/s00158-006-0087-x.

[10] O. Sigmund, Design of material structures using topology optimization, Ph.D. thesis, Technical University of Denmark Denmark (1994).

[11] O. Sigmund, On the Design of Compliant Mechanisms Using Topology Optimization, Mechanics of Structures and Machines 25 (4) (1997) 493–524. doi:10.1080/08905459708945415.

[12] J. Petersson, O. Sigmund, Slope constrained topology optimization, International Journal for Numerical Methods in Engineering 41 (8) (1998) 1417–1434. doi:10.1002/(sici)1097-0207(19980430)41:8¡1417::aid-nme344¿3.0.co;2-n.

[13] T. E. Bruns, D. A. Tortorelli, Topology optimization of non-linear elastic structures and compliant mechanisms, Computer Methods in Applied Mechanics and Engineering 190 (26-27) (2001) 3443–3459. doi:10.1016/s0045-7825(00)00278-4.

[14] B. Bourdin, Filters in topology optimization, International Journal for Numerical Methods in Engineering 50 (9) (2001) 2143–2158. doi:10.1002/nme.116.

[15] L. Ambrosio, G. Buttazzo, An optimal design problem with perimeter penalization, Calculus of Variations and Partial Differential Equations 1 (1) (1993) 55–69. doi:10.1007/bf02163264.

[16] R. B. Haber, C. S. Jog, M. P. Bendsøe, A new approach to variable-topology shape design using a constraint on perimeter, Structural Optimization 11 (1-2) (1996) 1–12. doi:10.1007/bf01279647.

[17] M. P. Bendsøe, Optimization of structural topology, shape, and material, Vol. 414, Springer, 1995.

[18] T. Borrvall, Topology optimization of elastic continua using restriction, Archives of Computational Methods in Engineering 8 (4) (2001) 351–385. doi:10.1007/bf02743737.

[19] F. Niordson, Optimal design of elastic plates with a constraint on the slope of the thickness function, International Journal of Solids and Structures 19 (2) (1983) 141–151. doi:10.1016/0020-7683(83)90005-7.

[20] M. Zhou, Y. K. Shyy, H. L. Thomas, Checkerboard and minimum member size control in topology optimization, Structural and Multidisciplinary Optimization 21 (2) (2001) 152–158. doi:10.1007/s001580050179.

[21] T. Borrvall, J. Petersson, Topology optimization using regularized intermediate density control, Computer Methods in Applied Mechanics and Engineering 190 (37-38) (2001) 4911–4928. doi:10.1016/s0045-7825(00)00356-x.

[22] T. A. Poulsen, A new scheme for imposing a minimum length scale in topology optimization, International Journal for Numerical Methods in Engineering 57 (6) (2003) 741–760. doi:10.1002/nme.694.

[23] Y. Y. Kim, G. H. Yoon, Multi-resolution multi-scale topology optimization — a new paradigm, International Journal of Solids and Structures 37 (39) (2000) 5529–5559. doi:10.1016/s0020-7683(99)00251-6.

[24] T. A. Poulsen, Topology optimization in wavelet space, International Journal for Numerical Methods in Engineering 53 (3) (2001) 567–582. doi:10.1002/nme.285.

[25] B. Bourdin, A. Chambolle, Design-dependent loads in topology optimization, ESAIM: Control, Optimisation and Calculus of Variations 9 (2003) 19–48. doi:10.1051/cocv:2002070.

[26] M. Y. Wang, S. Zhou, Phase field: a variational method for structural topology optimization, CMES-Computer Modeling in Engineering and Sciences 6 (6) (2004) 547.

[27] J. A. Sethian, A. Wiegmann, Structural boundary design via level set and immersed interface methods, Journal of Computational Physics 163 (2) (2000) 489–528. doi:10.1006/jcph.2000.6581.

[28] M. Y. Wang, X. Wang, D. Guo, A level set method for structural topology optimization, Computer Methods in Applied Mechanics and Engineering 192 (1-2) (2003) 227–246. doi:10.1016/s0045-7825(02)00559-5.

[29] G. Allaire, F. Jouve, A.-M. Toader, Structural optimization using sensitivity analysis and a level-set method, Journal of Computational Physics 194 (1) (2004) 363–393. doi:10.1016/j.jcp.2003.09.032.

[30] A. Díaz, O. Sigmund, Checkerboard patterns in layout optimization, Structural Optimization 10 (1) (1995)

40–45. doi:10.1007/bf01743693.

[31] J. K. Guest, Topology optimization with multiple phase projection, Computer Methods in Applied Mechanics and Engineering 199 (1-4) (2009) 123–135. doi:10.1016/j.cma.2009.09.023.

[32] Y. Li, H. Wang, K. Mo, T. Zeng, Reconstruction of simulation-based physical field by reconstruction neural network method (2018). doi:10.48550/ARXIV.1805.00528.

[33] I. Goodfellow, J. Pouget-Abadie, M. Mirza, B. Xu, D. Warde-Farley, S. Ozair, A. Courville, Y. Bengio, Generative adversarial nets, Advances in neural information processing systems 27 (2014).

[34] Y. Yu, T. Hur, J. Jung, I. G. Jang, Deep learning for determining a near-optimal topological design without any iteration, Structural and Multidisciplinary Optimization 59 (3) (2018) 787–799. doi:10.1007/s00158-018-2101-5.

[35] H. Sasaki, H. Igarashi, Topology optimization accelerated by deep learning, IEEE Transactions on Magnetics 55 (6) (2019) 1–5. doi:10.1109/tmag.2019.2901906.

[36] S. Rawat, M. H. H. Shen, A novel topology optimization approach using conditional deep learning (2019). doi:10.48550/ARXIV.1901.04859.

[37] I. Sosnovik, I. Oseledets, Neural networks for topology optimization, Russian Journal of Numerical Analysis and Mathematical Modelling 34 (4) (2019) 215–223. doi:10.1515/rnam-2019-0018.

[38] B. Li, C. Huang, X. Li, S. Zheng, J. Hong, Non-iterative structural topology optimization using deep learning, Computer-Aided Design 115 (2019) 172–180. doi:10.1016/j.cad.2019.05.038.

[39] L. Xue, J. Liu, G. Wen, H. Wang, Efficient, high-resolution topology optimization method based on convolutional neural networks, Frontiers of Mechanical Engineering 16 (1) (2021) 80–96. doi:10.1007/s11465-020-0614-2.

[40] C. Wang, S. Yao, Z. Wang, J. Hu, Deep super-resolution neural network for structural topology optimization, Engineering Optimization 53 (12) (2021) 2108–2121.

[41] Z. Zhang, Y. Li, W. Zhou, X. Chen, W. Yao, Y. Zhao, TONR: An exploration for a novel way combining neural network with topology optimization, Computer Methods in Applied Mechanics and Engineering 386 (2021) 114083. doi:10.1016/j.cma.2021.114083.

[42] S. Anwar, S. Khan, N. Barnes, A deep journey into super-resolution, ACM Computing Surveys 53 (3) (2021) 1–34. doi:10.1145/3390462.

[43] Z. Wang, J. Chen, S. C. H. Hoi, Deep learning for image super-resolution: a survey, IEEE Transactions on Pattern Analysis and Machine Intelligence 43 (10) (2021) 3365–3387. doi:10.1109/tpami.2020.2982166.

[44] B. Lim, S. Son, H. Kim, S. Nah, K. Mu Lee, Enhanced deep residual networks for single image super-resolution, in: Proceedings of the IEEE conference on computer vision and pattern recognition workshops, 2017, pp. 136–144.

[45] J. Yu, Y. Fan, J. Yang, N. Xu, Z. Wang, X. Wang, T. Huang, Wide activation for efficient and accurate image super-resolution (2018). doi:10.48550/ARXIV.1808.08718.

[46] C. Ledig, L. Theis, F. Huszár, J. Caballero, A. Cunningham, A. Acosta, A. Aitken, A. Tejani, J. Totz, Z. Wang, et al., Photo-realistic single image super-resolution using a generative adversarial network, in: Proceedings of the IEEE conference on computer vision and pattern recognition, 2017, pp. 4681–4690.

[47] C. Dong, C. C. Loy, X. Tang, Accelerating the Super-Resolution Convolutional Neural Network, in: B. Leibe, J. Matas, N. Sebe, M. Welling (Eds.), Computer Vision - ECCV 2016, Springer International Publishing, Cham,

2016, pp. 391–407.

[48] W. Shi, J. Caballero, F. Huszar, J. Totz, A. P. Aitken, R. Bishop, D. Rueckert, Z. Wang, Real-time single image and video super-resolution using an efficient sub-pixel convolutional neural network, in: Proceedings of the IEEE Conference on Computer Vision and Pattern Recognition (CVPR), 2016, pp. 1874–1883.

[49] W.-S. Lai, J.-B. Huang, N. Ahuja, M.-H. Yang, Fast and accurate image super-resolution with deep laplacian pyramid networks, IEEE Transactions on Pattern Analysis and Machine Intelligence 41 (11) (2019) 2599–2613. doi:10.1109/tpami.2018.2865304.

[50] W. Yang, X. Zhang, Y. Tian, W. Wang, J.-H. Xue, Q. Liao, Deep learning for single image super-resolution: a brief review, IEEE Transactions on Multimedia 21 (12) (2019) 3106–3121. doi:10.1109/tmm.2019.2919431.

[51] L. Zhou, S. Feng, A review of deep learning for single image super-resolution, in: 2019 International Conference on Intelligent Informatics and Biomedical Sciences (ICIIBMS), IEEE, 2019. doi:10.1109/iciibms46890.2019.8991477.

[52] C. Dong, C. C. Loy, K. He, X. Tang, Image super-resolution using deep convolutional networks, IEEE Transactions on Pattern Analysis and Machine Intelligence 38 (2) (2016) 295–307. doi:10.1109/tpami.2015.2439281.

[53] J. Kim, J. K. Lee, K. M. Lee, Accurate image super-resolution using very deep convolutional networks, in: Proceedings of the IEEE conference on computer vision and pattern recognition, 2016, pp. 1646–1654.

[54] M. Huang, W. Huang, Large-scale text classification with deeper and wider convolution neural network, International Journal of Simulation and Process Modelling 15 (1/2) (2020) 120. doi:10.1504/ijspm.2020.106977.

[55] K. He, X. Zhang, S. Ren, J. Sun, Deep residual learning for image recognition, in: Proceedings of the IEEE Conference on Computer Vision and Pattern Recognition (CVPR), 2016.

[56] S. Ioffe, C. Szegedy, Batch normalization: Accelerating deep network training by reducing internal covariate shift, in: International conference on machine learning, PMLR, 2015, pp. 448–456.

[57] K. Zhang, M. Sun, T. X. Han, X. Yuan, L. Guo, T. Liu, Residual networks of residual networks: multilevel residual networks, IEEE Transactions on Circuits and Systems for Video Technology 28 (6) (2018) 1303–1314. doi:10.1109/tcsvt.2017.2654543.

[58] G. E. Hinton, Rectified linear units improve restricted boltzmann machines vinod nair.

[59] H. Alqahtani, M. Kavakli-Thorne, G. Kumar, Applications of generative adversarial networks (GANs): an updated review, Archives of Computational Methods in Engineering 28 (2) (2019) 525–552. doi:10.1007/s11831-019-09388-y.

[60] K. He, X. Zhang, S. Ren, J. Sun, Delving deep into rectifiers: surpassing human-level performance on imagenet classification, in: Proceedings of the IEEE International Conference on Computer Vision (ICCV), 2015.

[61] C. Dong, C. C. Loy, K. He, X. Tang, Learning a Deep Convolutional Network for Image Super-Resolution, in: D. Fleet, T. Pajdla, B. Schiele, T. Tuytelaars (Eds.), Computer Vision - ECCV 2014, Springer International Publishing, Cham, 2014, pp. 184–199.

[62] J. Yang, J. Wright, T. S. Huang, Y. Ma, Image super-resolution via sparse representation, IEEE Transactions on Image Processing 19 (11) (2010) 2861–2873. doi:10.1109/tip.2010.2050625.

[63] R. Timofte, R. Rothe, L. Van Gool, Seven ways to improve example-based single image super resolution, in: Proceedings of the IEEE conference on computer vision and pattern recognition, 2016, pp. 1865–1873.

[64] Z. Wang, A. C. Bovik, H. R. Sheikh, E. P. Simoncelli, Image quality assessment: from error visibility to structural similarity, IEEE Transactions on Image Processing 13 (4) (2004) 600–612. doi:10.1109/tip.2003.819861.

[65] A. Hore, D. Ziou, Image quality metrics: PSNR vs. SSIM, in: 2010 20th International Conference on Pattern Recognition, IEEE, 2010. doi:10.1109/icpr.2010.579.

[66] R. Zeyde, M. Elad, M. Protter, On Single Image Scale-Up Using Sparse-Representations, in: J.-D. Boissonnat, P. Chenin, A. Cohen, C. Gout, T. Lyche, M.-L. Mazure, L. Schumaker (Eds.), Curves and Surfaces, Springer Berlin Heidelberg, Berlin, Heidelberg, 2012, pp. 711–730.

[67] G. I. N. Rozvany, Aims, scope, methods, history and unified terminology of computer-aided topology optimization in structural mechanics, Structural and Multidisciplinary Optimization 21 (2) (2001) 90–108. doi:10.1007/s001580050174.

[68] D. Tcherniak, Topology optimization of resonating structures using SIMP method, International Journal for Numerical Methods in Engineering 54 (11) (2002) 1605–1622. doi:10.1002/nme.484.

[69] Q. X. Lieu, J. Lee, Multiresolution topology optimization using isogeometric analysis, International Journal for Numerical Methods in Engineering 112 (13) (2017) 2025–2047. doi:10.1002/nme.5593.

[70] O. Sigmund, A 99 line topology optimization code written in matlab, Structural and Multidisciplinary Optimization 21 (2) (2001) 120–127. doi:10.1007/s001580050176.

[71] R. Tavakoli, S. M. Mohseni, Alternating active-phase algorithm for multimaterial topology optimization problems: a 115-line MATLAB implementation, Structural and Multidisciplinary Optimization 49 (4) (2013) 621–642. doi:10.1007/s00158-013-0999-1.

[72] S. Zhou, M. Y. Wang, Multimaterial structural topology optimization with a generalized cahn–hilliard model of multiphase transition, Structural and Multidisciplinary Optimization 33 (2) (2006) 89–111. doi:10.1007/s00158-006-0035-9.

[73] N. Olhoff, M. P. Bendsøe, J. Rasmussen, On CAD-integrated structural topology and design optimization, Computer Methods in Applied Mechanics and Engineering 89 (1-3) (1991) 259–279. doi:10.1016/0045-7825(91)90044-7.

[74] P. Duysinx, M. P. Bendsøe, Topology optimization of continuum structures with local stress constraints, International Journal for Numerical Methods in Engineering 43 (8) (1998) 1453–1478. doi:10.1002/(sici)1097-0207(19981230)43:8¡1453::aid-nme480¿3.0.co;2-2.